Master Thesis

Improvement of Particle Identification for Electron Neutrino Event Selection Using New T2K Near Detectors

（T2K実験新型検出器群での電子ニュートリノ事象選別のための粒子識別手法の改善）

January 24, 2024

Department of Physics, Graduate School of Science
The University of Tokyo
東京大学大学院理学系研究科物理学専攻

Wataru Okinaga
沖永和平

Abstract

The T2K experiment is a long baseline neutrino oscillation experiment conducted in Japan. The near detector ND280 and far detector Super-Kamiokande measure the neutrino beam produced from the accelerators in J-PARC. The T2K experiment aims to observe leptonic CP violation by precisely measuring the neutrino oscillation probabilities. CP conservation in neutrino oscillation was rejected at a 90% confidence level from the previous data analysis. The ν_e cross-section is one of the dominant systematic uncertainties and it must be measured precisely to improve the experiment sensitivity. Measuring the ν_e cross-section is challenging since only about 1% of the neutrinos in the beam are ν_e.

T2K has upgraded ND280 to further constrain the uncertainty on neutrino interactions. Measuring the ν_e cross-section is one of the motivations of the upgrade. SuperFGD, which is one of the new detectors, has been installed and will start collecting neutrino data in 2024. There was a study on selecting the ν_e components in the beam using SuperFGD. However, it was done for events where the produced electrons stop in SuperFGD which are only 1/3 of the ν_e events. In this thesis, the particle identification method is extended for events where the electron escapes SuperFGD by combining the information from the surrounding detectors. Based on the simulation, the selection efficiency and purity for all the ν_e events are estimated to be 23% and 69%, respectively. With the same data amount, the number of selected ν_e events is three times larger than in the previous study. This result leads to a further reduction of the statistical error, which is crucial for the ν_e cross-section measurement.

Contents

Chapter 1

Neutrino Physics

1.1   Neutrino Oscillation

In the Standard Model, quarks and leptons are the elementary particles and their inter-
actions are described with quantum field theory. The fermions are shown in Table 1.1
and they interact by exchanging bosons shown in Table 1.2. There are three interactions
in the Standard Model: strong, electromagnetic and weak.

The difference between matter and antimatter, called CP violation, is not imple-
mented in the Standard Model. This is one of the keys to explain why the universe has
less antimatter than matter. The CP violation in the quark sector was first observed in
1964 [1] and many experiments have been conducted until now. Compared to quarks,
there are few studies on the CP violation in the lepton sector. Measuring neutrino oscil-
lation is currently the only way to observe leptonic CP violation.

Neutrinos are neutral leptons which only interact through the weak interaction. Neu-
trinos have three flavor eigenstates which are the election neutrino (ν_e), muon neutrino
(ν_μ) and tau neutrino (ν_τ). They can also be characterized by their mass eigenstates
(ν_1, ν_2, ν_3). Flavor states can be described as superpositions of mass states. The mixing
matrix U is defined as

$$
\begin{pmatrix} \nu_e \\ \nu_\mu \\ \nu_\tau \end{pmatrix} = U \begin{pmatrix} \nu_1 \\ \nu_2 \\ \nu_3 \end{pmatrix} = \begin{pmatrix} U_{e1} & U_{e2} & U_{e3} \\ U_{\mu1} & U_{\mu2} & U_{\mu3} \\ U_{\tau1} & U_{\tau2} & U_{\tau3} \end{pmatrix} \begin{pmatrix} \nu_1 \\ \nu_2 \\ \nu_3 \end{pmatrix},
\tag{1.1}
$$

which is called the Pontecorvo-Maki-Nakagawa-Sakata (PMNS) matrix. The widely used
parameterization of the PMNS matrix is

$$
U = \begin{pmatrix} 1 & 0 & 0 \\ 0 & \cos\theta_{23} & \sin\theta_{23} \\ 0 & -\sin\theta_{23} & \cos\theta_{23} \end{pmatrix} \begin{pmatrix} \cos\theta_{13} & 0 & \sin\theta_{13}e^{-i\delta_{CP}} \\ 0 & 1 & 0 \\ -\sin\theta_{13}e^{i\delta_{CP}} & 0 & \cos\theta_{13} \end{pmatrix} \begin{pmatrix} \cos\theta_{12} & \sin\theta_{12} & 0 \\ -\sin\theta_{12} & \cos\theta_{12} & 0 \\ 0 & 0 & 1 \end{pmatrix},
\tag{1.2}
$$

where $\theta_{12}, \theta_{13}, \theta_{23}(0 \leq \theta_{ij} \leq \pi/2)$ are the mixing angles and $\delta_{CP}(-\pi < \delta_{CP} \leq \pi)$ is the
CP-violating phase.

Because of this feature, a neutrino can change its flavor by itself. This phenomenon
is known as neutrino oscillation. The oscillation probability from ν_α to ν_β ($\alpha, \beta = e, \mu, \tau$)
when it propagates through a vacuum is calculated as

$$P(\nu_\alpha \to \nu_\beta) = \delta_{\alpha\beta} - 4 \sum_{j=1}^{3} \sum_{i=1}^{j} Re[U_{\alpha i} U_{\beta i}^* U_{\alpha j}^* U_{\beta j}] \sin^2 \left(\frac{\Delta m_{ij}^2 L}{4E} \right)$$
$$\pm 2 \sum_{j=1}^{3} \sum_{i=1}^{j} Im[U_{\alpha i} U_{\beta i}^* U_{\alpha j}^* U_{\beta j}] \sin \left(\frac{\Delta m_{ij}^2 L}{2E} \right), \quad (1.3)$$

where Δm_{ij}^2 is the squared mass difference $m_i^2 - m_j^2$, E is the neutrino energy and L is the flight length. The last $\pm$ term in Eq. 1.3 will be positive for neutrinos and negative for antineutrinos. Thus, the difference in oscillation probabilities between neutrinos and antineutrinos is

$$\Delta P_{\alpha\to\beta} \equiv P(\nu_\alpha \to \nu_\beta) - P(\bar\nu_\alpha \to \bar\nu_\beta) = 4 \sum_{j=1}^{3} \sum_{i=1}^{j} Im[U_{\alpha i} U_{\beta i}^* U_{\alpha j}^* U_{\beta j}] \sin \left(\frac{\Delta m_{ij}^2 L}{2E} \right). \quad (1.4)$$

Leptonic CP violation can be probed by measuring $\Delta P_{\alpha\to\beta}$. Note that $P(\nu_\alpha \to \nu_\alpha)$, which is called the survival probability, cannot be used in this study. It is because $U_{\alpha i} U_{\alpha i}^* U_{\alpha j}^* U_{\alpha j} = |U_{\alpha i} U_{\alpha j}|^2$ is real and the survival probability is

$$P(\nu_\alpha \to \nu_\alpha) = P(\bar\nu_\alpha \to \bar\nu_\alpha) = 1 - 4 \sum_{j=1}^{3} \sum_{i=1}^{j} |U_{\alpha i} U_{\alpha j}|^2 \sin^2 \left(\frac{\Delta m_{ij}^2 L}{4E} \right), \quad (1.5)$$

which means $\Delta P_{\alpha\to\alpha}$ is always 0.

Neutrino oscillation is measured by detecting neutrinos far from the neutrino source. There are mainly four kinds of neutrino sources that are used for oscillation measurements: The sun, secondary cosmic rays, accelerators and reactors. The energy of the ν_e produced by the sun is around 10 MeV or less and is much smaller than the muon mass of 106 MeV/c^2. This means that when a ν_e changes into ν_μ, it does not have the energy to produce a muon and can no longer be detected. The $\bar\nu_e$ from reactors have energy of few MeV and cannot be detected when they turn into $\bar\nu_\mu$ for the same reason. These neutrinos cannot be used to measure $P(\nu_e \to \nu_\mu)$ or $P(\bar\nu_e \to \bar\nu_\mu)$. $P(\nu_\mu \to \nu_e)$ and $P(\bar\nu_\mu \to \bar\nu_e)$ of neutrinos from secondary cosmic rays, called atmospheric neutrinos, has been studied in experiments such as the Super-Kamiokande experiment [2]. To measure neutrino oscillation in different conditions, neutrino beam from accelerators is also used in experiments such as the T2K experiment [3] and the NOvA experiment [4]. Although there are some ideas proposed to design beamlines for $\nu_e(\bar\nu_e)$ such as neutrino factories [5], so far only a $\nu_\mu(\bar\nu_\mu)$ beam has been developed. $P(\nu_\mu \to \nu_\tau)$ is difficult to measure since the neutrino energy threshold for producing τ is 3.5 GeV which is difficult to achieve. In addition, τ cannot be directly detected because of its extremely short lifetime ($\sim$300 fs). Therefore, $\Delta P_{\mu\to e}$ is currently the only measurable value to investigate CP violation using accelerator neutrinos. This is calculated as

$$\Delta P_{\mu\to e} = -2 \sin\delta_{CP} \cos\theta_{13} \sin 2\theta_{12} \sin 2\theta_{13} \sin 2\theta_{23}$$
$$\times \sin \left(\frac{\Delta m_{12}^2 L}{4E} \right) \sin \left(\frac{\Delta m_{13}^2 L}{4E} \right) \sin \left(\frac{\Delta m_{23}^2 L}{4E} \right). \quad (1.6)$$

From this, the condition for $\Delta P_{\mu \to e} \neq 0$ is

$$\theta_{ij} \neq 0, \quad m_i \neq m_j, \quad \delta_{CP} \neq 0, \pi. \tag{1.7}$$

The ordering of the mass eigenstates is also important. It must be determined to further understand the properties of neutrinos. Also, the mixing angles and CP-violating phase depends on the mass hierarchy. The past experiments determined that $\Delta m_{21}^2 > 0$ [6] and $|\Delta m_{32}^2| > \Delta m_{21}^2$ [3]. From this, there are two possible orderings which are $m_1 < m_2 < m_3$ called normal hierarchy and $m_3 < m_1 < m_2$ called inverted hierarchy.

Table 1.1. Fermions in the Standard Model and their EM charge.

	EM charge	particle		
quark	2/3	u (up)	c (charm)	t (top)
	−1/3	d (down)	s (strange)	b (bottom)
lepton	−1	e	μ	τ
	0	ν_e	ν_μ	ν_τ

Table 1.2. Bosons in the Standard Model and the interaction they produce.

particle	interaction
g	strong
$W^\pm, Z$	weak
γ	electromagnetic

1.2 Neutrino Interaction and Detection

Oscillation measurement is done by detecting neutrino interaction. A neutrino interacts with an atom through the weak interaction. There are two types of interactions: The Charged Current (CC) interaction which exchanges a charged W boson and the Neutral Current (NC) interaction which exchanges a neutral Z boson. The main difference is that the CC interaction produces a charged lepton corresponding to the flavor of the neutrino while NC does not. These interactions can be sub-categorized with the particles they produce and their cross section depends on the neutrino energy. CC interactions have three common interactions around a few GeV which the energy range in which accelerator neutrinos are currently produced. The first is CC quasi-elastic scattering (CCQE) which results in a charged lepton and a nucleon. The second is known as resonant pion production (RES) in which a lepton and a $\Delta(1232)$ baryon are produced. $\Delta(1232)$ immediately decays into a pion and nucleon. The last is deep inelastic scattering (DIS) where the neutrino interacts with a quark in the target nucleus and causes a jet that produces multiple hadrons such as pions. Figure 1.1 shows the interaction diagram and Fig. 1.2 shows the cross section of each interaction.

The lepton from a CC interaction is mainly used to tag neutrino events. By identifying which lepton was produced, it is possible to determine the flavor of the neutrino.

For the CCQE interaction, the neutrino energy can be reconstructed as a classical two-body scattering. Ignoring nuclear binding energy, the neutrino energy with a given lepton momentum is

$$E_\nu^{QE} = \frac{m_p^2 - m_n^2 - m_l^2 + 2m_n E_l}{2(m_n - E_l + p_l \cos\theta_l)} \tag{1.8}$$

where m_p, m_n and m_l are the mass of proton, neutron and lepton respectively and E_l, p_l and θ_l are lepton energy, momentum and scattering angle with respect to the neutrino direction.
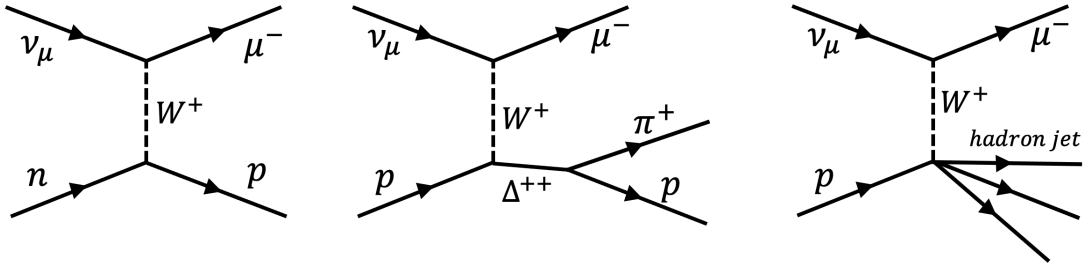
Figure 1.1. The diagrams of muon neutrino CCQE (left), CC RES (middle) and CC DIS (right).
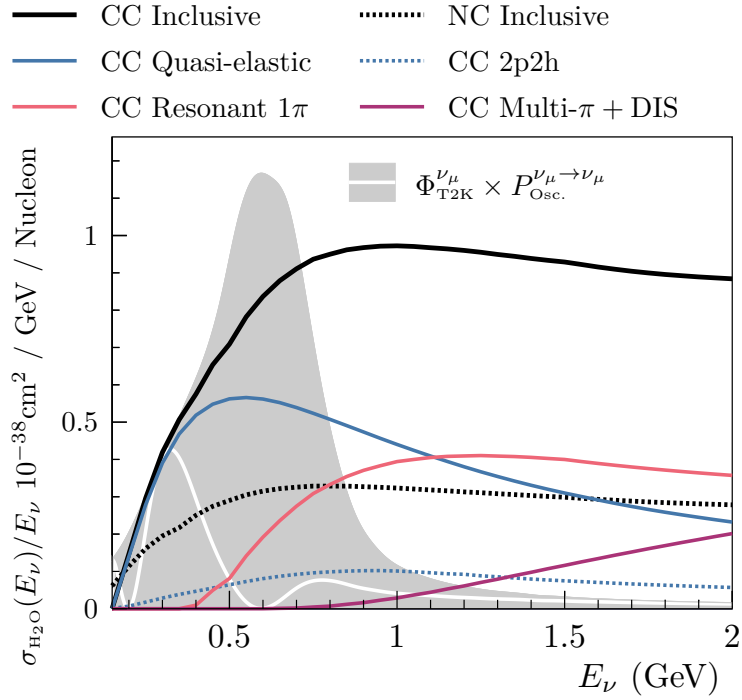
Figure 1.2. The muon neutrino-water cross section for various interactions [7]. The interaction of each curve is as follows: All the CC interactions summed up (black), all NC interactions (dashed black), CCQE (blue), CC 2p2h which is a scattering of correlated nucleon pairs (dashed blue), CC RES (red) and CC interactions which produce multiple pions (purple). These cross sections (σ_{H_2O}) are predicted in NEUT, which is a neutrino interaction simulation library. The gray region shows the energy of the muon neutrino flux produced in the T2K experiment ($\Phi^{\nu_\mu}_{T2K}$), and the white line is the flux with the survival probability multiplied.

Chapter 2

T2K Experiment

The T2K (Tokai to Kamioka) experiment is a long baseline neutrino oscillation experiment conducted in Japan. The accelerators in Japan Proton Accelerator Research Complex (J-PARC) generate ν_μ and $\bar{\nu}_\mu$ beams. The near detector ND280 and far detector Super-Kamiokande (SK) detect those neutrinos at distances of 280 m and 295 km from the beam production point, respectively. The main goal is to precisely measure the mixing angles, squared mass difference and CP-violating phase by observing the oscillation channels. Channels $\nu_\mu(\bar{\nu}_\mu) \to \nu_e(\bar{\nu}_e)$ are sensitive to θ_{13} and δ_{CP} while $\nu_\mu(\bar{\nu}_\mu) \to \nu_\mu(\bar{\nu}_\mu)$ are sensitive to θ_{23} and Δm_{23}^2.

2.1 J-PARC Accelerator and Neutrino Beamline

J-PARC is located in Ibaraki prefecture and consists of three accelerators: The linear accelerator (LINAC), the rapid cycling synchrotron (RCS) and the main ring synchrotron (MR). LINAC, RCS and MR gradually accelerate protons to 400 MeV, 3 GeV and 30 GeV, respectively. With these accelerators, a proton spill is produced every 2.48 s[*]. It consists of eight bunches with 580 ns intervals (Fig. 2.1). These protons are oriented towards SK with magnets and sent to a graphite target. Hadrons, mainly charged pions, are produced when the proton beam strikes the target. Three magnetic horns focus the pions and send them to a decay volume to let them decay into neutrinos. The schematic view of the neutrino beamline is shown in Fig. 2.2. The neutrino beam mode is selected by changing the horn current: Forward horn current (FHC) for neutrinos and reversed horn current (RHC) for antineutrinos. The dominant pion decay channels for FHC and RHC modes are

$$\begin{aligned} \pi^+ &\to \mu^+ + \nu_\mu, \\ \pi^- &\to \mu^- + \bar{\nu}_\mu. \end{aligned} \tag{2.1}$$

Kaon decays are dominant at an energy range higher than 3 GeV:

$$\begin{aligned} K^+ &\to \mu^+ + \nu_\mu, \ \ K^+ \to \pi^0 + \mu^+ + \nu_\mu, \\ K^- &\to \mu^- + \bar{\nu}_\mu, \ \ K^- \to \pi^0 + \mu^- + \bar{\nu}_\mu. \end{aligned} \tag{2.2}$$

---

[*]This spill interval is shortened after the beam upgrade discussed in Sec. 2.5.

A beam dump located downstream of the decay volume stops hadrons and muons. A muon monitor called MUMON is placed behind the dump. It provides information on the beam position by measuring energetic muons penetrating the dump.
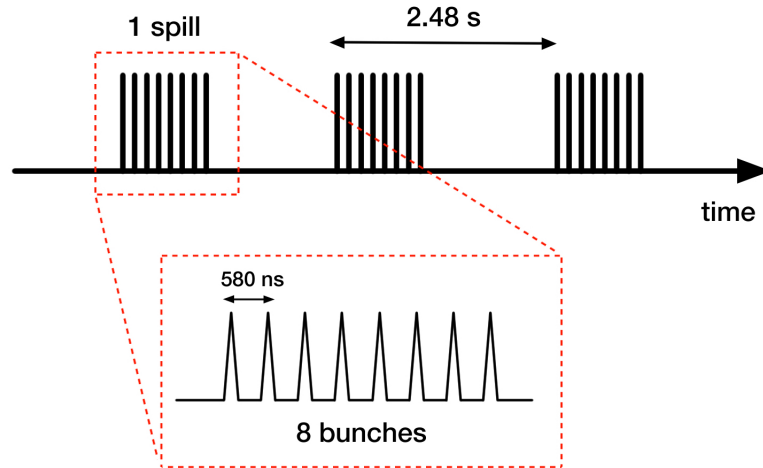
Figure 2.1. Beam spills and their bunch structure.
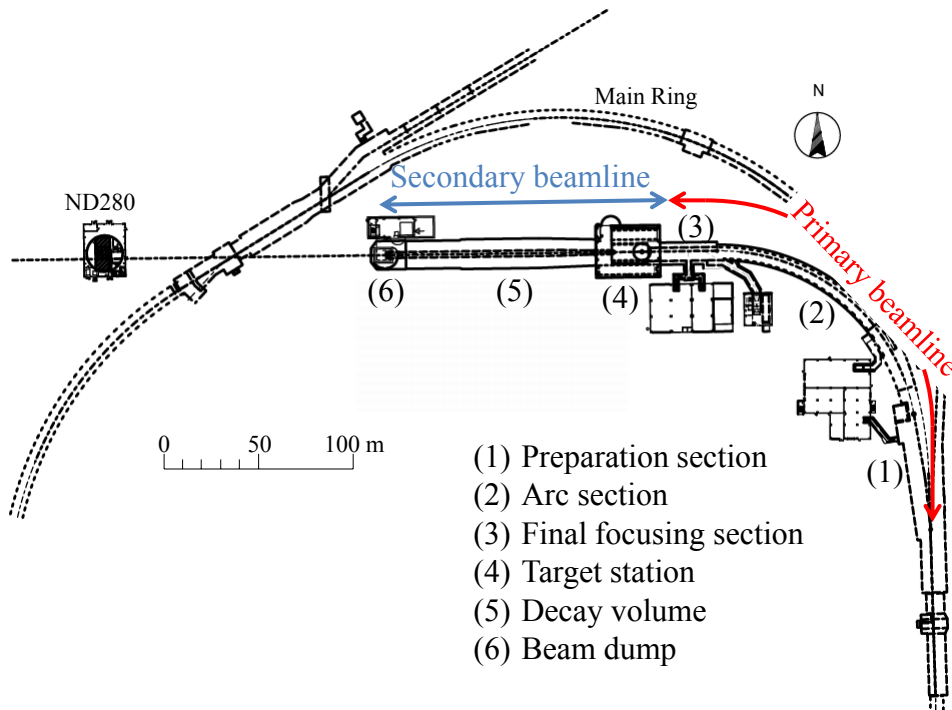
Figure 2.2. Overview of the neutrino beamline [8].

The neutrino beam direction is shifted 2.5° away from SK. This narrows the energy spectrum of neutrinos flying towards SK because of the kinematic limitation. This is known as the "off-axis method" which is used to adjust the energy peak to maximize the oscillation probability and to also reduce high energy neutrino background. With this off-axis angle, the neutrino energy peak is at 0.6 GeV. The oscillation probability and neutrino energy are shown in Fig. 2.3.

Figure 2.4 shows the predicted FHC flux at the near detector. There is $\bar{\nu}_\mu$ contamination with approximately 10% of the amount of ν_μ. This is because negative and positive hadrons cannot be completely selected with the magnetic horn. Also, there are ν_e and $\bar{\nu}_e$ produced from kaon and muon decays which are

$$K^+ \to \pi^0 + e^+ + \nu_e, \ \mu^+ \to \bar{\nu}_\mu + e^+ + \nu_e,$$
$$K^- \to \pi^0 + e^- + \bar{\nu}_e, \ \mu^- \to \nu_\mu + e^- + \bar{\nu}_e. \tag{2.3}$$

The ν_e flux is about 1% of that of ν_μ and the mean energy is 1.28 GeV.
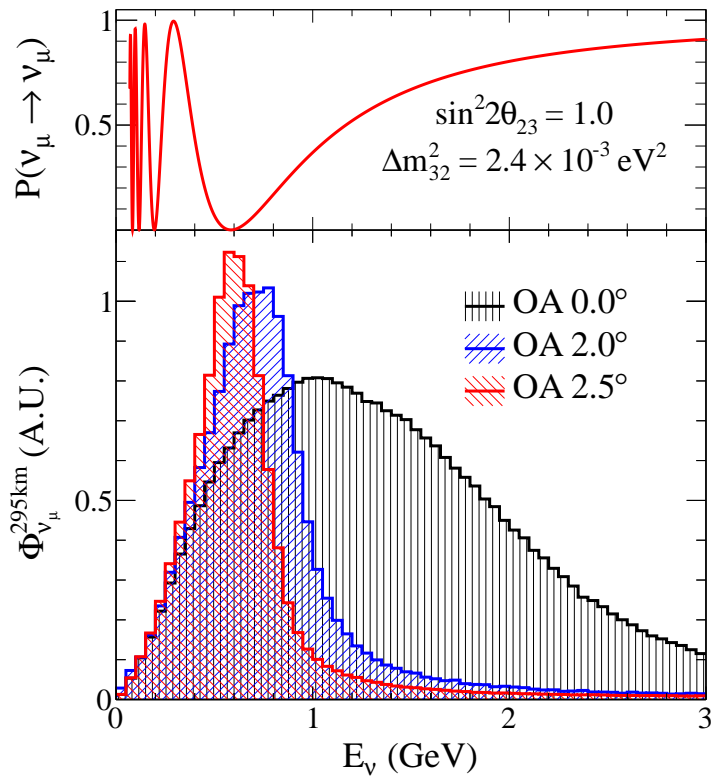
Figure 2.3. The predicted neutrino survival probability and T2K neutrino flux at distance 295 km from the proton target [8]. OA is the off-axis angle.
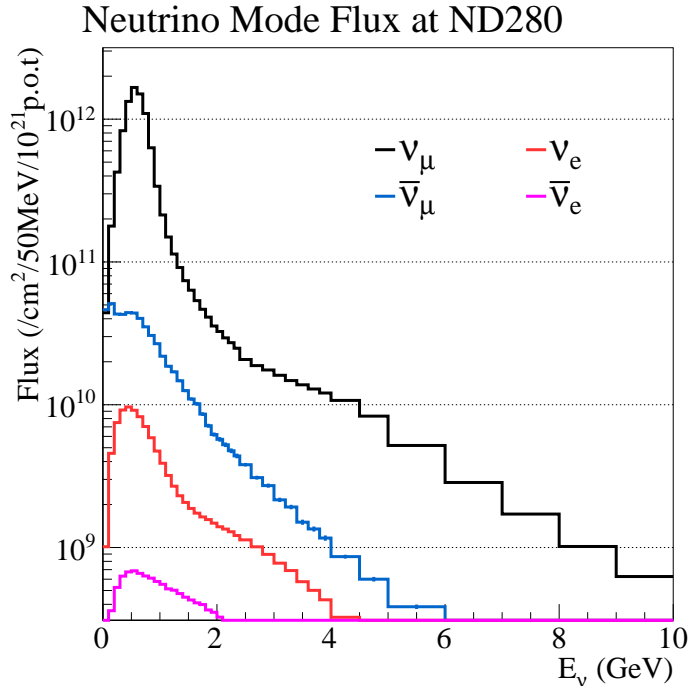
Figure 2.4. Predicted FHC mode flux at the near detector [9]. The unit p.o.t is the number of protons hitting the target (proton-on-target).

2.2   Near Detector

ND280 is an off-axis near detector placed in the same direction as SK, 280 m away from the beam target. Figure 2.5 shows the overview of ND280. ND280 contributes to oscillation analysis by constraining the uncertainties of neutrino flux and the neutrino interaction model. It is composed of several sub-detectors. Fine-Grained-Detector (FGD) is a neutrino interaction point detector with a high resolution. Time projection chambers (TPCs) are set in front of and behind FGD to track particles from FGD. Pi-zero detector (P0D) is placed at the upstream side of ND280 to measure NC interactions that produce π^0. Electromagnetic calorimeters (ECals) surround these detectors to detect outgoing particles. A magnet that was used in the UA1 experiment covers all of these sub-detectors and applies a 0.2 T magnetic field.

2.2.1   Fine-Grained-Detector (FGD)

FGD [10] is a high-resolution scintillator tracker which works as a neutrino target. It is used to detect the neutrino interaction point and track particles produced from the interaction. There are two FGDs, and from the upstream, they are named FGD1 and FGD2. 184 cm × 0.96 cm × 0.96 cm scintillator bars are aligned to make a layer perpendicular to the beam. Each layer consists of 192 bars and the direction of the bars in the odd and even layers are perpendicular to each other (Fig. 2.6). FGD1 has 30 layers. On the other hand, FGD2 has 14 layers and 6 water layers to measure neutrino-water interaction.
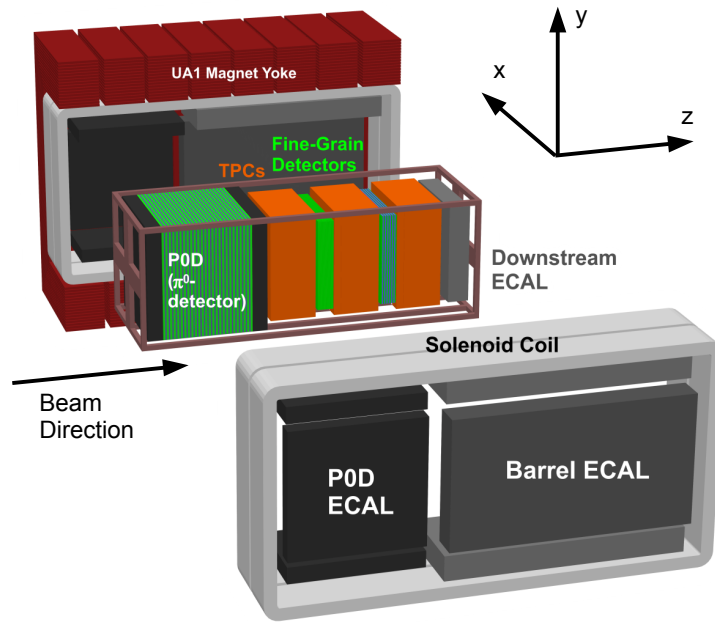
Figure 2.5. Overview of the current ND280.
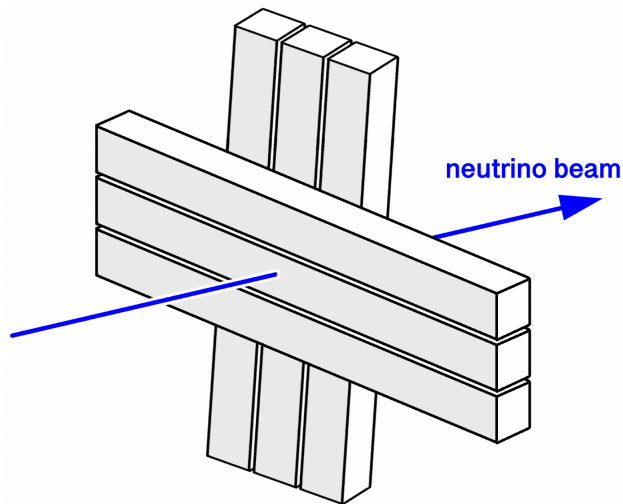
Figure 2.6. The scintillator bars in FGD.

2.2.2 Time Projection Chamber (TPC)

TPC [11] tracks particles from FGD and measures their momentum and charge from their curvature caused by the magnetic field. It is also capable of identifying particles such as muons, protons and electrons by measuring the energy loss per length. Figure 2.7 shows the schismatic view of TPC. Three TPCs are placed so that each FGD is sandwiched in TPCs. From the upstream, these TPCs are named TPC1, TPC2 and TPC3. Each TPC
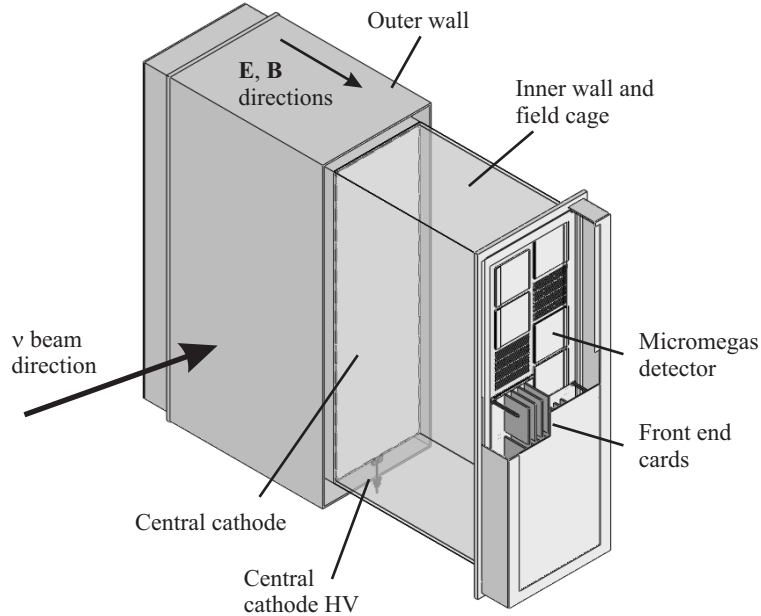
Figure 2.7. The basic structure of TPC [11].

contains gas which is a mixture of Ar(95%), CF_4(3%) and iso-C_4H_{10}(2%). The gas is sealed in a gas-tight box, and the box is separated with a central cathode which applies high-voltage. The overall size of the TPC is $2.3 \times 2.4 \times 1.0$ m^3. When a charged particle goes into TPC, it ionizes the gas molecules on its way. An electric field is applied to make the ionized electrons drift to the MicroMEGAS modules which detect them. Each module has 48×36 channels to cover a 36×34 cm^3 sensitive area, and Each TPC has 2×6 modules on both sides. The drift length can be calculated from the timing information given by FGD. 3D tracking is done by combining the hit position and drift length.

2.2.3 Pi-Zero Detector (P0D)

P0D [12] consists of layers of scintillator bars and lead sheets to detect NC interaction which emits π^0 such as

$$\nu_\mu + p \rightarrow \nu_\mu + p + \pi^0. \tag{2.4}$$

It also has water layers to measure the cross section of water-neutrino NC interaction which produces π^0.

2.2.4 Electromagnetic Calorimeter (ECal)

ECals [13] surround the sub-detectors and measure the energy of outgoing electrons and gamma rays by detecting their shower. This ability is also used to distinguish electrons and muons. There are three ECals based on their region: P0D-ECal which surrounds P0D, barrel-ECal which surrounds FGDs and TPCs, and Ds-ECal which is placed at the most downstream part of ND280. Since barrel-ECal and Ds-ECal surround the tracking

14

detectors in ND280, the two are referred to as tracker-ECal. ECals have a similar structure to FGDs with layers of scintillator bars. The difference is that there are lead sheets between layers. The thickness of the lead sheets of the tracker-ECal (P0D-ECal) is 1.75 mm (4.00 mm). The cross-section of the scintillator bars is 40 × 10 mm, and there is a 2 mm diameter hole along the bar to insert a wavelength shifting (WLS) fiber. The scintillation light is collected and propagated through the fibers and detected with multi-pixel photon counters (MPPCs) attached at the end of the fibers. There are 31 scintillator-lead layers in barrel-ECal and 34 in Ds-ECal, which are 10 radiation length (X_0) and 11 X_0, respectively. P0D-ECal has only 6 layers which is 4.3 X_0 since P0D itself does the shower detection.

2.3   Far Detector

Super-Kamiokande (SK) is the far detector of T2K located in Gifu prefecture, 295 km away from the beam target. Same as ND280, SK detects neutrinos from J-PARC. However, the detection method is quite different. SK is a cylindrical water tank with a diameter of 39.3 m and height of 41.4 m, filled with 50 kton of water. There is an inner tank with a diameter of 33.8 m and a height of 36.2 m. 20-inch photo-multiplier tubes cover the tank wall to detect Cherenkov radiation caused by charged particles from neutrino interaction. The ring-like structure of the signals from the Cherenkov radiation provides information on the particles' direction, energy and flavor. The outer tank is used to veto cosmic-ray muons.

2.4   Recent Results

T2K has collected data from 2009 to 2018 in neutrino (antineutrino) mode with beam exposure at $1.97 \times 10^{21} (1.63 \times 10^{21})$ proton-on-target (POT). T2K concluded that the 90% confidence interval of δ_{CP} is $[-3.01, -0.52]$ for normal mass hierarchy and $[-1.74, -1.07]$ for inverted mass hierarchy [3]. The statistical error is the dominant uncertainty in this result. Furthermore, there is a 6.0% systematic uncertainty on the $\nu_e/\bar{\nu}_e$ event rate ratio. This factor is important since the objective is to measure $\Delta P_{\mu \to e}$ by detecting $\nu_e(\bar{\nu}_e)$ turned from $\nu_\mu(\bar{\nu}_\mu)$. The largest fraction of this uncertainty is the uncertainty of the $\nu_e/\bar{\nu}_e$ interaction model. T2K uses $\nu_e/\bar{\nu}_e$ cross section estimated from that of $\nu_\mu/\bar{\nu}_\mu$. This estimation has a 3.0% uncertainty, and a precise measurement of $\nu_e/\bar{\nu}_e$ cross section is needed.

T2K has attempted to measure ν_e cross section by detecting ν_e components in the neutrino beam with ND280 [9]. Data of 11.92×10^{20} POT in FHC mode was analyzed. Using NEUT 5.3.2, which is a neutrino interaction simulation library, the ν_e selection efficiency and purity were estimated to be 26% and 54%, respectively. The measured ν_e cross-section in FHC mode was

$$\sigma_{\nu_e} = 6.62 \pm 1.32 (\text{stat}) \pm 1.30 (\text{syst}) \times 10^{-39} \text{ cm}^2/\text{nucleon} \qquad (2.5)$$

in the limited phase space which was $p > 300$ MeV/c, $\theta \leq 45°$. The result is not used in oscillation analysis because the statistical and systematic errors are both around 20%. As
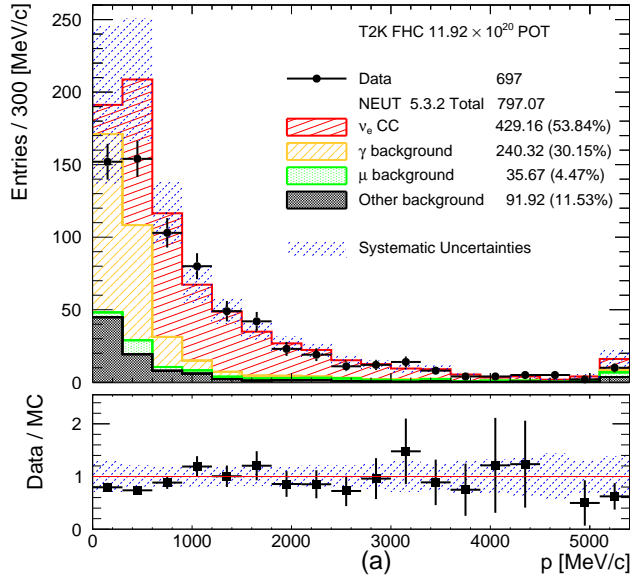
Figure 2.8. The momentum distribution of selected electron candidates [9].

shown in Fig. 2.8, there is a large background contribution caused by photons, especially at the momentum range below 600 MeV/c. This energy region is important because T2K measures the neutrino oscillation at energy 600 MeV, and a more efficient way to reject the photon background is needed. Also, electrons can be emitted in a phase space outside of this analysis. Since SK has a 4π acceptance, ν_e cross section must be measured in the same phase space. Particle identification methods for detecting high angle electrons and rejecting gamma background are needed to precisely measure ν_eCC cross-section.

2.5   T2K-II

Because statistical uncertainty is dominant in δ_{CP} measurement, the accelerator and neutrino beamline are being upgraded for more data. T2K plans to increase the beam power up to 1.3 MW with a spill interval of 1.16 s. The magnetic horns will be also upgraded to separate neutrinos and antineutrinos more efficiently.

While gaining statistics, the systematic uncertainty must also be reduced. By upgrading ND280 and measuring neutrino interaction more precisely, T2K aims to reduce the systematic uncertainty from 6.0% to 4.0% which is needed to achieve 3σ confidence in the CP violation measurement. Details of the upgraded ND280 are discussed in the next chapter.

Chapter 3

ND280 Upgrade

3.1 Limitations of the Current ND280

T2K has been measuring neutrino-nucleus interaction with ND280 to constrain the uncertainties in oscillation analysis. Using FGD, TPC and ECal, interactions with various final states can be measured. TPC plays a key role in particle identification and momentum reconstruction with its 1 mm spatial resolution and 10% momentum resolution for particles with 1 GeV/c momentum.

However, particles with large emission angles with respect to the beam direction leave only a short track in TPC, or do not even enter TPC. Analyzing these events is challenging since there is little or no information available from TPC. Furthermore, since scintillator bars are used in FGD, particles flying along the direction of the bars are difficult to track. These limitations cause an efficiency decrease in the high-angle region.

The limitation on the sensitivity to low momentum particles is also a problem. Reconstructing a track in FGD requires 3 points (6 hits). This means a charged particle must travel at least 6 cm to be detected. This length corresponds to protons with momentum of 600 MeV/c. However it is predicted that there are many events with protons with less momentum. To further constrain the uncertainty of the neutrino interaction model, lowering the threshold is needed.

Moreover, ND280 cannot distinguish ν_e CC interaction from $\gamma \to e^- e^+$ conversion in the low energy region. This makes gamma the dominant background in ν_e detection. As discussed in Sec. 2.4, precise ν_e cross-section measurement is crucial to oscillation analysis.

3.2 New Detectors

To deal with these limitations, the upgraded ND280 [14] was designed to satisfy the following conditions:

- Tracking ability with 4π acceptance.

- High efficiency in reconstructing low momentum particles.

- Capability of distinguishing ν_e interaction from gamma conversion.
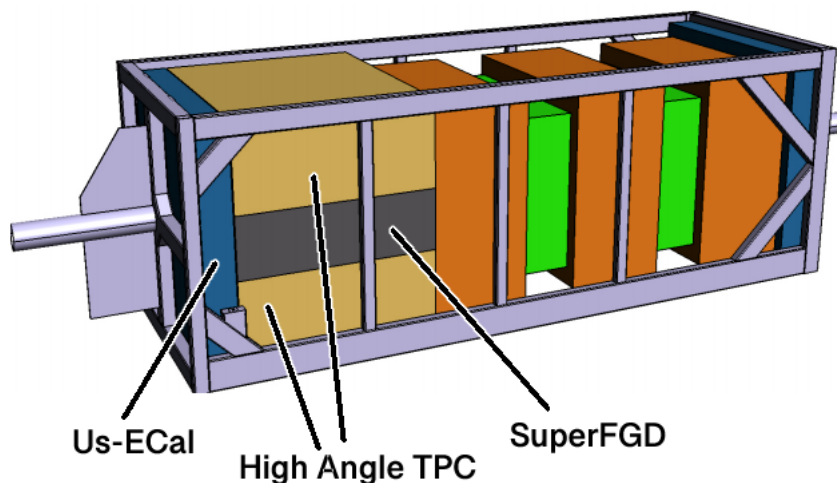
Figure 3.1. The overview of the ND280 after upgrade.

After the upgrade, P0D was replaced with a scintillator tracker SuperFGD with 2 TPCs above and below it. These TPCs are called High Angle TPCs (HATs). These three detectors are covered with six Time-of-Flight (ToF) scintillator layers. The upstream calorimeter of P0D is reused as Us-ECal (4.9 X_0), which is set in the most upstream of ND280. Figure 3.1 shows the overview of the upgraded ND280.

3.2.1 SuperFGD

SuperFGD is a neutrino target in the upgraded ND280 (Fig. 3.2). It is composed of 192 $\times$ 56 $\times$ 182 scintillator cubes with the size of $1 \times 1 \times 1$ cm^3, produced by UNIPLAST Co. in Russia. Cubes are made of polystyrene doped with 1.5% paraterphenyl and 0.01% POPOP. White reflecting layers are formed by chemical etching to prevent light from spreading to neighboring cubes. Three holes perpendicular to each other are made and wavelength shifting (WLS) fibers are inserted to collect scintillation light. These WLS fibers are Y-11 (200) produced by KURARAY CO., LTD.

WLS fibers are connected to multi-pixel photon counters (MPPCs) to detect the light. The MPPC type used in SuperFGD is S13360-1325PE produced by Hamamatsu Photonics K.K. The sensitive area of each MPPC is 1.3×1.3 mm^2. 8×8 MPPCs are mounted on printed circuit boards (PCBs) shown in Fig. 3.3. The total number of readout channels is 55,888.

For readout electronics, Cherenkov Imaging Telescope Integrated Read Out Chip (CITIROC) is adopted. This is a frontend ASIC capable of reading 32 MPPC channels at the same time. In CITIROC, the signal is processed in two ways which are high gain and low gain. It also gives the information on how long the signal was over the threshold which is called the Time-over-Threshold. Eight CITIROC chips are mounted on a frontend board (FEB) and fourteen FEBs are connected to an optical concentrator board (OCB). Sixteen OCBs are connected to a master clock board.

The light from WLS fibers is measured from one side. There are LED calibration

modules attached on the opposite side from the side with the MPPCs. These modules inject LED light into each channel for calibration (Fig. 3.4). The modules were designed to inject light in multiple channels at once since there are about 60,000 channels in SuperFGD.

3.2.2 High Angle TPC (HAT)

There are two HATs placed over and under SuperFGD. Their role is to track and identify particles with large emission angles from SuperFGD. The basic structure and contained gas are the same as TPCs in the current ND280. The main difference is that the overall size is $2.0 \times 0.8 \times 1.8$ m and there are 4×2 MicroMEGAS modules on both sides.

3.2.3 Time-of-Flight Detector (ToF)

Shown in Fig. 3.5, six Time-of-Flight (ToF) detectors cover SuperFGD and HATs. They are capable of precisely measuring the crossing time of particles to reject charged particles from outside. Each ToF plane is composed of scintillator bars with MPPC directly attached on both ends with no light guide. The size of the bars along the beam direction is $200 \times 1 \times 12$ cm^2 while the bars perpendicular to the beam are $230 \times 1 \times 12$ cm^2. By reading out the signal from both ends, the timing resolution is around 150 ps.
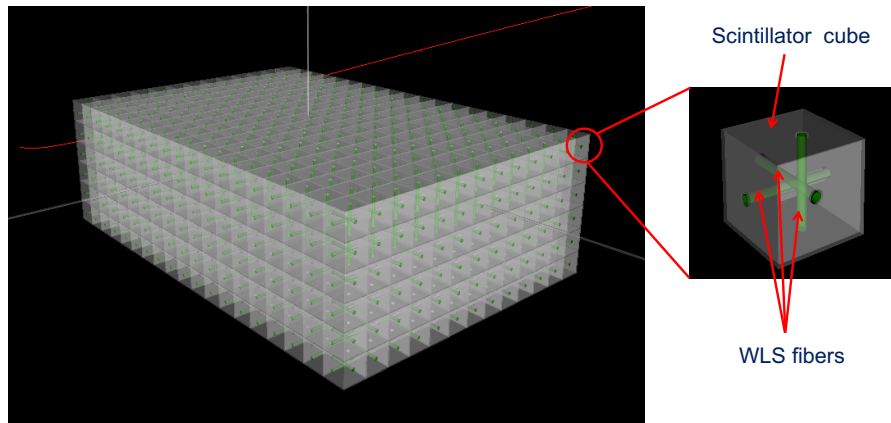
Figure 3.2. The schematic view of the SuperFGD structure [14].

Figure 3.3. 8×8 MPPCs mounted on a PCB.
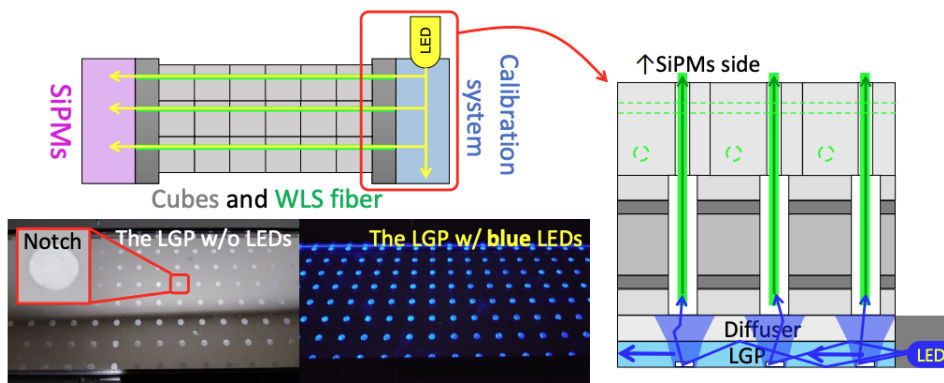
Figure 3.4. The overview of the LED calibration module [15].
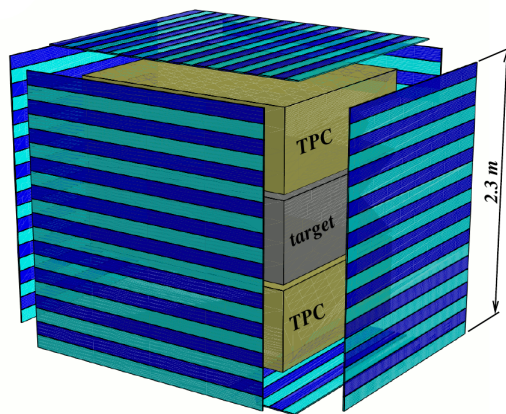
Figure 3.5. The schematic view of the ToF with SuperFGD and HAT inside [14].
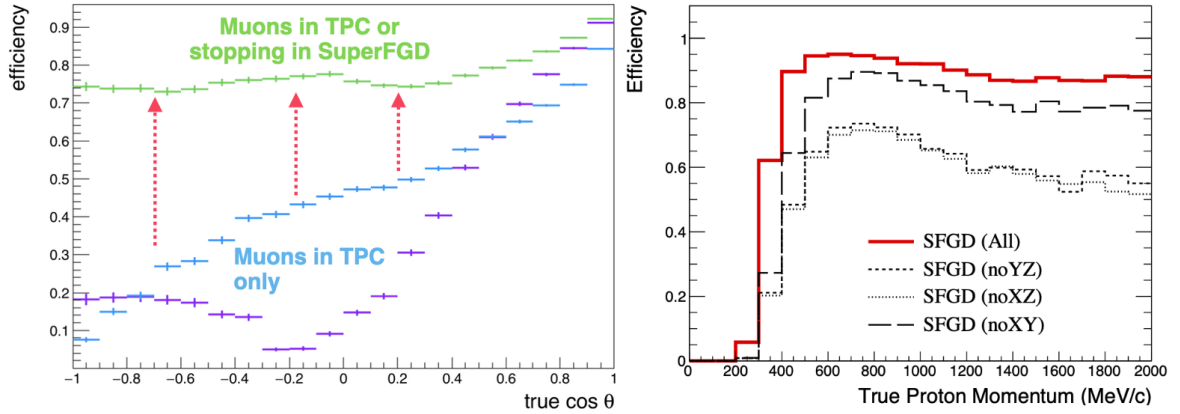
Figure 3.6. Left: Muon tracking efficiency as a function of the muon emission angle θ [17]. Right: The proton tracking efficiency in SuperFGD as a function of the proton momentum with readouts for three or two directions [14].

3.3 Expected Performance

Figure 3.6 shows the muon and proton tracking efficiency after the upgrade. Because of the two HATs above and under SuperFGD and the fine granularity of SuperFGD itself, the efficiency for events with muon emission angle around $\cos\theta < 0.5$ has dramatically improved. For proton track reconstruction, the momentum threshold has been lowered to 300 MeV/c.

Figure 3.7 shows a simulated ν_eCC interaction event display in SuperFGD. SuperFGD is capable of precisely reconstructing showers. Discrimination for electron and other particles including gammas has been studied with this ability [16]. It is capable of rejecting 99% of gamma while maintaining the electron efficiency at 80%.
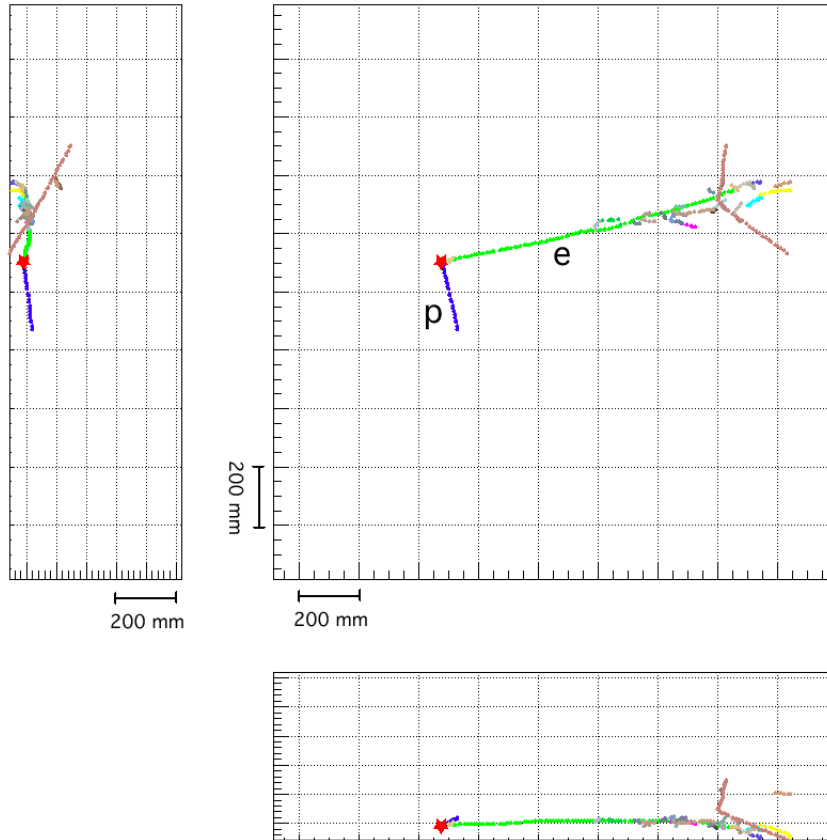
Figure 3.7. A simulated ν_eCC interaction event display in SuperFGD seen from three directions. The red star is the neutrino interaction point. The colored lines show the reconstructed tracks.

3.4 Construction of SuperFGD

The construction of SuperFGD started in October 2022. During the assembly, the scintillator cubes were aligned inside the SuperFGD box. Fishing lines were used to hold the cubes in place. The fishing lines were pulled out and WLS fibers were inserted one by one. WLS fibers were checked by injecting LED light and measuring them from the opposite side so that they do not have cracks that cause light decrease. After the fibers were checked, the PCBs were attached. In parallel, the LED calibration modules were also constructed and a quality check was done for each module. With all PCBs and LED modules attached, the SuperFGD box was covered with black sheets to prevent light from coming in. Cables were attached after the sheets were secured. The light tightness and dead channels were checked for each PCB. No light leakage was found in this inspection. Some dead channels were found but solved by replacing the PCBs, and all 55,888 channels were alive. The construction ended in April 2023. Figure 3.8 shows some photos taken during the construction.

After constructing SuperFGD, the commissioning before installation started. Al-
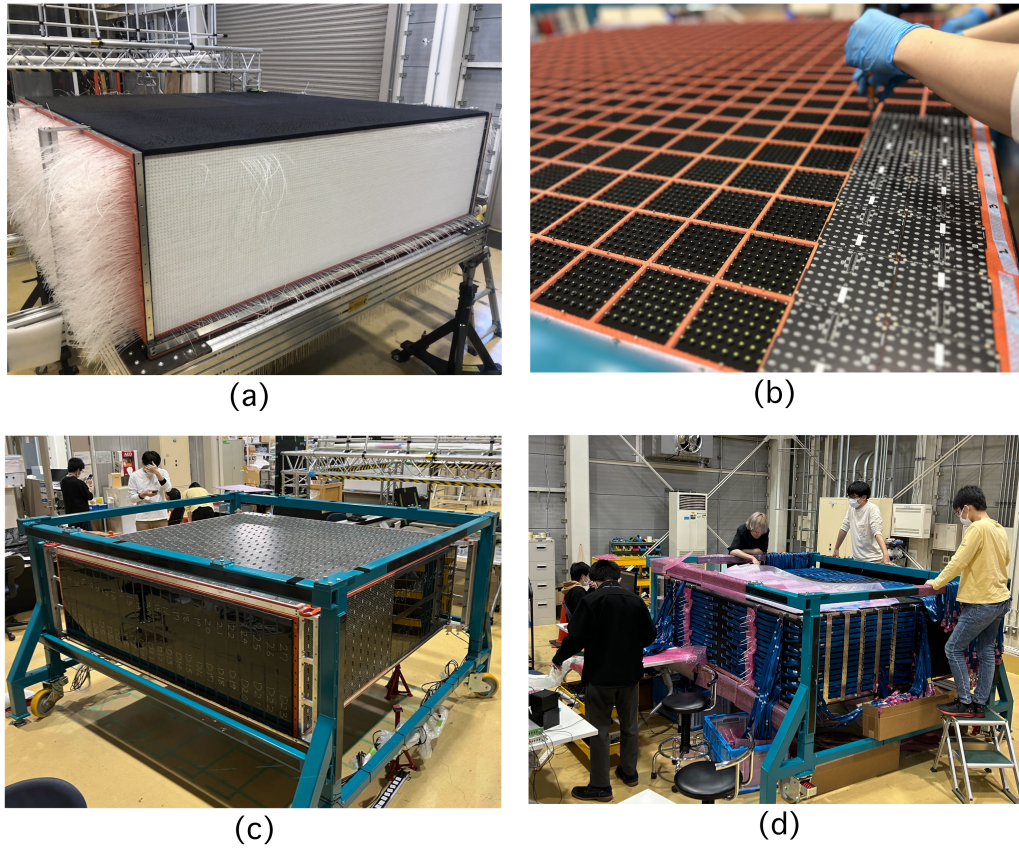
Figure 3.8. (a) All cubes aligned in the SuperFGD box. The white fibers are fishing lines inserted to hold the cubes in place. (b) WLS fibers are inserted and PCBs are being attached. (c) All PCBs and LED calibration modules are installed. (d) Cables are all attached and the light tightness and dead channels are being checked.

though half of the electronics were not prepared, LED and cosmic muon data were studied in the commissioning. It was confirmed that the LED modules worked as expected, and the light yield of the MPPCs were uniform. The attenuation length of the fibers was measured and the result agreed with the manufacturer specification.

3.5 Status of the Upgrade

As shown in Fig. 3.9, SuperFGD was installed in ND280 in October 2023, and the beam data taking started for data quality check. Although the upper HAT is still not ready, the ToF planes and the bottom HAT are also installed and taking beam data. Figure 3.10 shows a neutrino event candidate taken during the beam time. The data taken cannot be used for analysis since there are missing electronics and the calibration is not finished yet. However, this is a huge milestone for the T2K experiment.

Figure 3.9. SuperFGD being installed in ND280 with a crane.
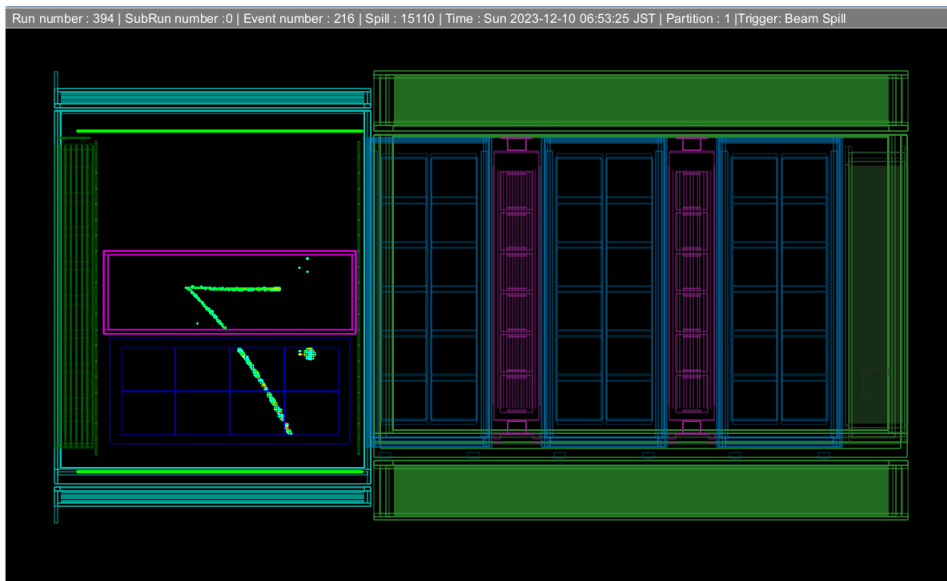
Figure 3.10. A neutrino event candidate taken during the beam time.

3.6 Motivation of this Thesis

Precise measurement of δ_{CP} from neutrino oscillation is one of the keys to understand the asymmetry of matter and antimatter in the universe. Since δ_{CP} is measured by detecting ν_e oscillated from ν_μ, the understanding of ν_e cross section is important. However, there are only a handful of experiments that measured ν_e cross-section and all of the results are limited with low statistics and high background rate. The recent measurements of ν_e cross section are summarised in Table 3.1. In the T2K experiment, only 1% of the neutrinos in the beam are ν_e, and selecting those events is challenging. Furthermore, gammas coming from outside the detector mimic ν_e events. This makes it even more difficult to find ν_e events. There was an attempt to measure the ν_e cross-section using ND280 before the upgrade but the statistical and systematic errors were both 20% [9]. The ν_e selection efficiency and purity were 26% and 54%, respectively. Gammas with low energy were the dominant background.

One of the motivations for the detector upgrade is to precisely measure the ν_e cross-section. There was a study on selecting ν_e CC events in SuperFGD [16], but it only focused on the particle identification performance in SuperFGD itself. The study was done for events where the primary lepton from the CC interaction stops in SuperFGD. However, it is predicted that for 2/3 of the ν_eCC events, the primary electron escapes SuperFGD. The study needed a lot of data to reduce the statistical error since it was limited to stopping events. Moreover, the selection did not use information from other detectors and the study still needs improvement.

The main topic of this thesis is to improve the current ν_e selection into a more practical method. The particle identification is improved by optimizing the particle discriminator of SuperFGD itself, and also combining the outputs from other detectors. By extending the selection for ν_e CC events where the electron escapes SuperFGD, this study aims to reduce the statistical error with less data. The study in [16] will be referred to as the "previous study" in this thesis. The contents of this thesis are as follows: In Chapter 4, the simulation sample and reconstruction are explained. In Chapter 5, the updated particle identification in SuperFGD is discussed. Finally, in Chapter 6, the ν_eCC selection method and its result are discussed.

Table 3.1. Recent ν_e and $\bar{\nu}_e$ cross section measurements.

experiment	year	average energy $(\nu_e, \bar{\nu}_e)$	target
MINERvA [18]	2016	3.6 GeV (only ν_e)	CH
T2K [9]	2020	1.28 GeV, 1.98GeV	CH
MicroBooNE [19]	2022	768 MeV, 961 MeV	Ar

Chapter 4

Simulation Samples and Reconstruction

4.1 Simulation Samples

Two types of Monte Carlo (MC) simulation samples, which are neutrino interaction samples and particle gun samples, are used in this thesis. There are three steps in generating these samples. First, the particle type, momentum, and starting position are decided. Next, the behavior of each particle is simulated with Geant4. Finally, the response of each detector is simulated. These two samples differ in the first step. The neutrino interaction samples use NEUT to generate the particles produced from the interaction while the particle gun samples have a single primary particle whose starting point is inside SuperFGD.

4.1.1 Neutrino Interaction Samples

Neutrino interaction samples were generated using NEUT 5.6.0, with 1×10^{21} POT at FHC (neutrino) mode. The events are categorized by whether the neutrino interaction vertex is inside the SuperFGD fiducial volume (FV). The FV is defined as the inner scintillator cube region except for the outer two layers whose thickness is 2cm. The neutrino interaction outside the FV includes interaction in the other detectors and the magnet. The mass of the magnet is 900 tons and most of the interaction in ND280 occurs in it. The background particles produced in interactions outside the FV are also simulated. The events in the FV are then sub-categorized by their flavor and interaction type, $\nu_\mu(\bar{\nu}_\mu)$CC, $\nu_e(\bar{\nu}_e)$CC and NC interaction. The event rates of each category are shown in Table 4.1. This study aims to select ν_eCC in SuperFGD FV, and the other events are considered as background events.

Table 4.2 shows the detector to which the primary electron from the CC interaction escapes. "SuperFGD" means the electron stops in SuperFGD and "Other" means that the electron escapes SuperFGD but doesn't reach to another sub-detector. Note that this is only about the primary electron, and if an electromagnetic shower occurs, other electrons from the shower may end up in another detector. In the previous study, only event samples where the primary charged leptons stop in SuperFGD were used. However, only 34% of the electron from ν_eCC interaction stops in SuperFGD.

Table 4.1. Event rate of the neutrino interaction samples for 1×10^{21} POT at FHC mode.

	ν_μCC	$\bar{\nu}_\mu$CC	ν_eCC	$\bar{\nu}_e$CC	NC	Out FV
Event rate	156397	4918	2701	259	51717	3216686

Table 4.2. The detector which the primary electron escapes to.

	SuperFGD	TPC1	HAT	Us-ECal	P0D-ECal	Other
Ratio	34%	30%	21%	8%	4%	3%

4.1.2 Particle Gun Samples

Particle gun samples are generated for the training of particle identification. Particle gun samples of five types of particles which are mainly produced from neutrino interaction were prepared: e^-, μ^-, π^+, p and γ. The direction and starting point in SuperFGD of each particle were uniformly distributed. The initial momentum was also uniformly distributed in the range shown in Table 4.3. Each momentum range covers 90% of the momentum distribution generated by NEUT.

Table 4.3. Momentum range of each particle gun sample.

	e^-	μ^-	π^+	p	γ
Momentum [GeV]	[0, 3.5]	[0, 2.5]	[0, 1.5]	[0, 1.5]	[0, 1.5]

4.1.3 Geant4 Simulation

The Geant4 package [20] simulates the trajectory of particles from the given momentum and detector geometry. It is capable of simulating the particles' interaction process such as the position, timing and energy loss. Using the Geant4 package, the geometry information on SuperFGD, the other sub-detectors, and the magnet are implemented in the simulation. The geometry parameters in SuperFGD are shown in Table 4.4.

Table 4.4. Parameters of the SuperFGD geometry.

Parameter	Value
Number of cubes	$192 \times 56 \times 184$
Cube length (Coating thickness)	10.27 mm (0.1mm)
Hole radius	0.75 mm
Fiber radius	0.50 mm

4.1.4 Detector Response Simulation

With the interaction between particles and detectors simulated, the next step is to simulate the detector response. For SuperFGD and ECal, first the scintillator response such as the conversion from energy to photon and the cross-talk, which is a phenomenon where the photon escapes to the neighboring scintillators, are simulated. Next, the response of WLS fibers such as the attenuation of the light is calculated. Finally the response of MPPCs and electronics are simulated such as the photon detection efficiency and time digitizer step. For TPCs, the ionization of electrons and their drift are simulated. After that, the response of the MicroMEGAS is simulated. Table 4.5 shows some parameters used to simulate the response of SuperFGD. The format of the simulated response is the same as the real data.

Table 4.5. Parameters used for simulating the detector response in SuperFGD.

Parameter	Value
Photons per MeV	320
Cube cross-talk rate along an axis	3.4%
Long component of the fiber attenuation	4634 mm
Short component of the fiber attenuation	332 mm
Dark count rate	3000 Hz
Photon detection efficiency	25%
Discriminator threshold	1.2 p.e.
Time digitizer step (Jitter)	1.25 ns (0.1 ns)

4.2 Reconstruction and Particle Identification

The reconstruction in ND280 has two steps. First, the signals are processed through each of the sub-detector reconstructions. Next, the reconstructed objects in the sub-detectors are combined to form a complete picture of an event in ND280. This step is called global reconstruction. Particle identification (PID) is applied after the reconstruction.

4.2.1 SuperFGD Reconstruction

For the SuperFGD reconstruction, 2D projections of MPPC hits are used. Since SuperFGD has readouts for three directions, 3D hits can be built with the 2D hit data. Neighboring hits are put together into groups. These grouped hits, including cross-talk hits, are merged and fitted into nodes with a pattern recognition algorithm. Each node has information on the position, timing, direction and energy loss. Objects with two or more nodes are classified as tracks, otherwise clusters. The node at the end of a track is called a vertex. The detail of the reconstruction flow is described in [16]. Figure 4.1 shows the track reconstruction efficiency for muon particle gun samples. The efficiency is 100% at any momentum. The PID method will be discussed in the next chapter.
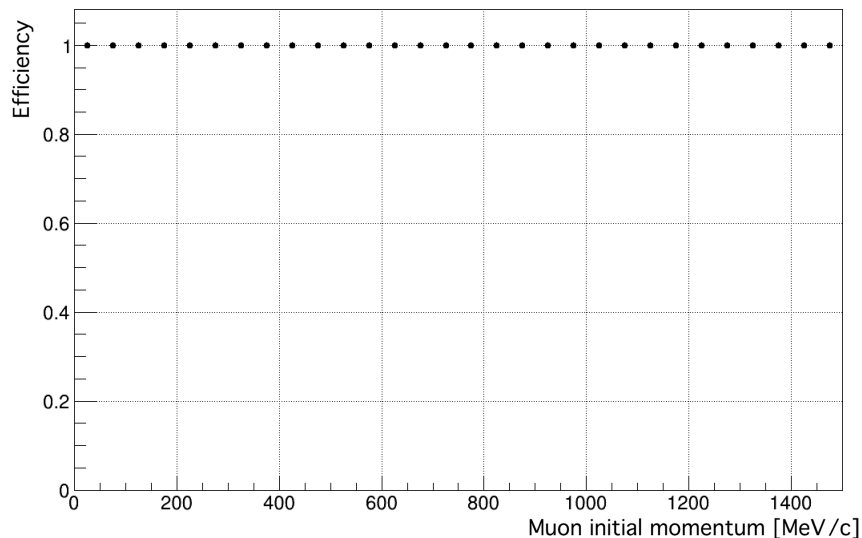
Figure 4.1. The track reconstruction efficiency in SuperFGD as a function of the initial momentum for muons.

4.2.2 TPC/HAT Reconstruction

For TPC and HAT, there is a 2D hit projection of MicroMEGAS pads in one direction. The hits are grouped as tracks using a pattern recognition algorithm. After that, the drift distance is reconstructed. This is done by taking the timing of the hit in SuperFGD which is the nearest to the extrapolated TPC track. This timing information is used as the starting time of the TPC track, and the drift distance is calculated from the drift speed. With this, the 3D position of the track is reconstructed. If there are no appropriate hits in SuperFGD, hits in FGD or ECal are used to find the starting time. The spatial resolution in TPC is around 1 mm. Figure 4.2 shows the track reconstruction efficiency for muon particle gun samples. The average efficiency is around 96%. The efficiency loss is due to muons that went through the edge of TPC. The reconstruction of HAT is not implemented yet but it is expected that the performance should be similar to TPC since the basic structure is the same.

TPC is capable of measuring each track's curvature and energy loss, and the momentum can be calculated with the curvature. The momentum resolution is 10% at 1 GeV/c. With the measured momentum, the energy loss per length dE/dx can be estimated for each particle hypothesis. By comparing the measured and expected dE/dx, the particle can be identified. The comparison for the particle i hypothesis is

$$\delta_i = \frac{dE/dx^M - dE/dx_i^E}{\sigma^M} \tag{4.1}$$

where dE/dx^M and dE/dx_i^E are the measured and expected energy loss for particle i and σ^M is the uncertainty of the measured energy loss. Figure 4.3 shows the measured δ_e for electrons and muons. The likelihood for each particle is calculated as

$$L_i = \frac{\exp(-\delta_i^2/2)}{\sum_{\alpha=e,\mu,\pi,p} \exp(-\delta_\alpha^2/2)}. \tag{4.2}$$

29
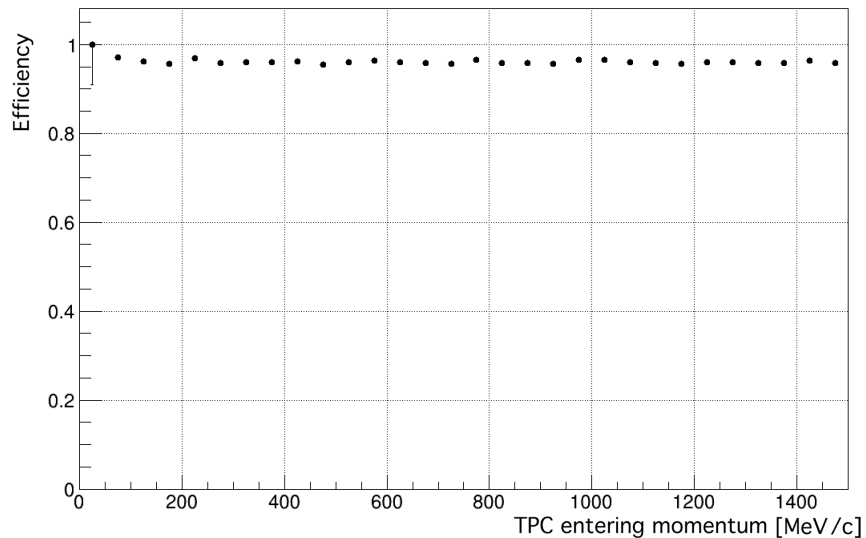
Figure 4.2. The track reconstruction efficiency in TPC as a function of the entering momentum for muons. The starting points of muons are in SuperFGD.

Whether using δ_i or L_i does not much affect the PID performance. In this study L_i is used since it is easier to analyze with the PID output of other detectors.

4.2.3 ECal Reconstruction

Unlike TPC, the objective of ECal is reconstructing showers and their energy. ECal has readouts for two directions making it capable of reconstructing 3D hits. Hits within two layers are grouped into clusters since showers can cause isolated hits.

For ECal, a neural network distinguishes whether the cluster is electromagnetic (EM) shower-like or minimal ionizing particle (MIP) like. This also estimates the energy loss in ECal. The inputs are:

- The ratio between the width and length of the cluster.

- The charge ratio between the layers with the highest and lowest charge.

- The root mean square of the charge hit distribution.

- The charge ratio between the the front and back quarter of the cluster.

The output is the log likelihood ratio $R_{\mathrm{MIP/EM}}$ which is positive for shower-like and negative for MIP-like. Figure 4.4 shows the measured $R_{\mathrm{MIP/EM}}$ for electrons and muons.
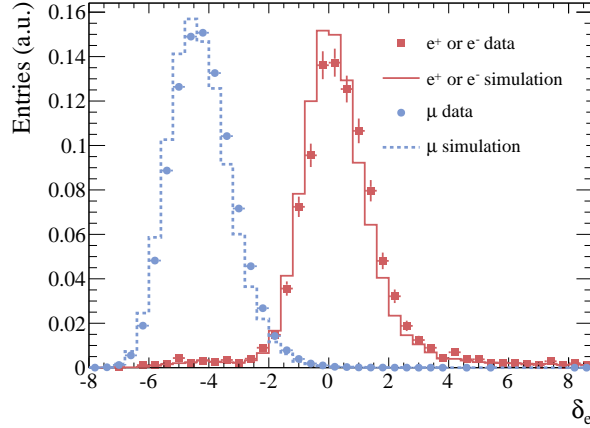
Figure 4.3. The δ_e for electrons and muons measured in TPC [21].
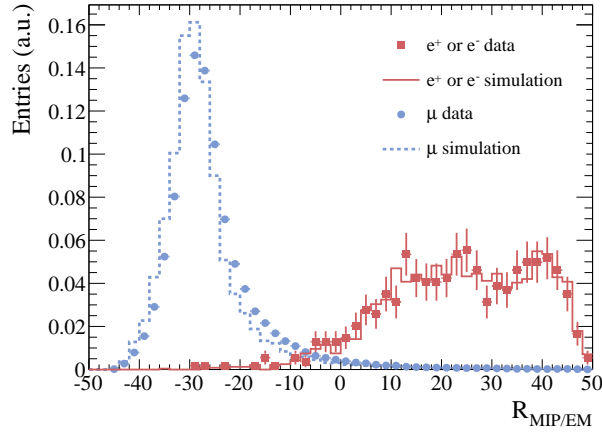
Figure 4.4. The $R_{\mathrm{MIP/EM}}$ for electrons and muons measured in ECal [21].

4.2.4 Global Reconstruction

The objects reconstructed in each detector are combined in this step. The RecPack Kalman Filter [22] is used to extrapolate tracks and decide whether they match or not. Matched tracks are merged into a single track. Pairs of tracks are matched one by one, and if they are merged, they are refitted with the Kalman Filter. Figure 4.5 and Fig. 4.6 show the matching efficiency between SuperFGD and TPC for muon particle gun samples as a function of the SuperFGD nodes and TPC hits. The average efficiency is 95%. About 20 hits in TPC are needed for 90% efficiency. This corresponds to a quarter of a MicroMEGAS module or 1/8 of the TPC. Figure 4.7 shows the matching efficiency between SuperFGD and Us-ECal and the average matching efficiency is 96%. Figure 4.8 shows the matching efficiency between TPC and tracker-ECal and the average matching efficiency is 95%. PID with the global reconstruction is discussed in Sec. 6.4.
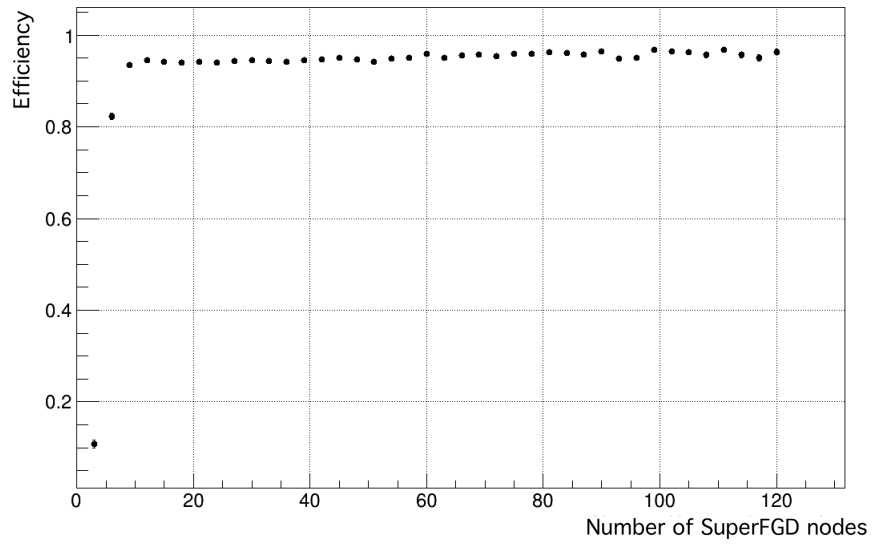
Figure 4.5. The track matching efficiency between SuperFGD and TPC as a function of the number of SuperFGD nodes for muons.
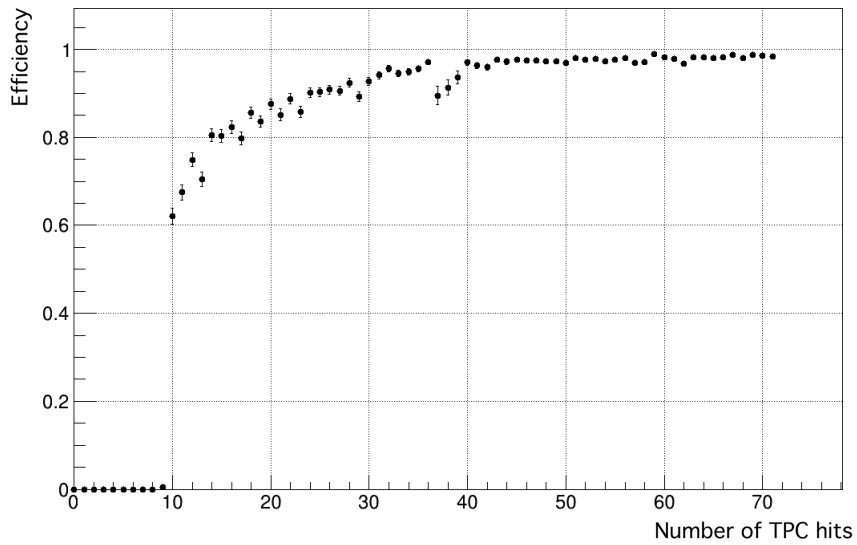
Figure 4.6. The track matching efficiency between SuperFGD and TPC as a function of the number of TPC hits for muons.
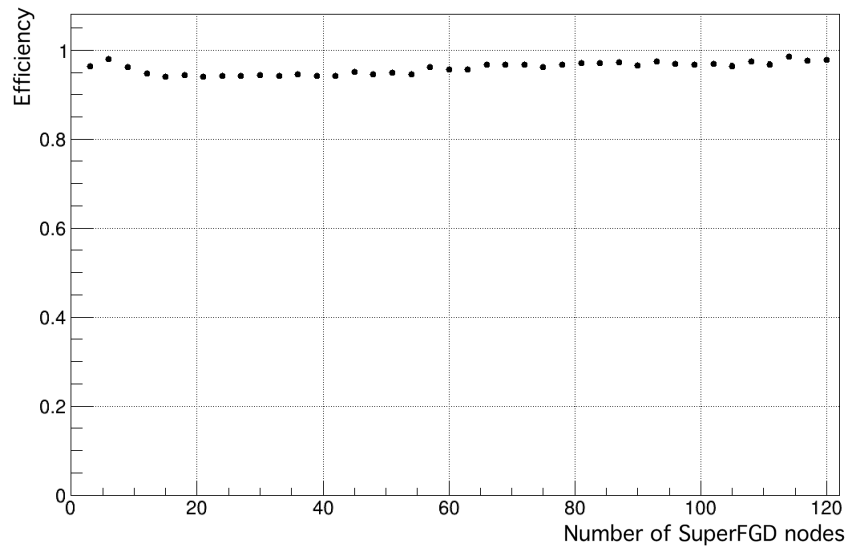
Figure 4.7. The matching efficiency between SuperFGD tracks and Us-ECal clusters as a function of the number of SuperFGD nodes for muons.
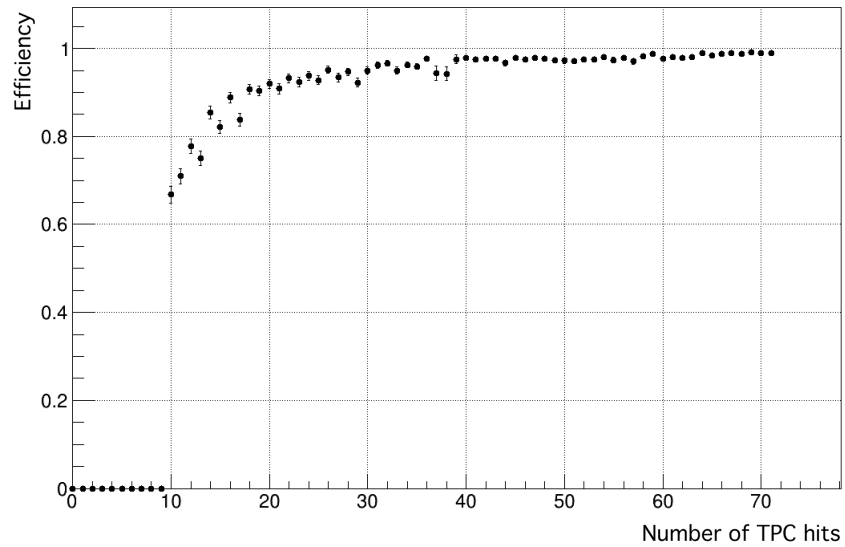
Figure 4.8. The matching efficiency between TPC tracks and tracker-ECal clusters as a function of the number of TPC hits for muons.

Chapter 5

Electron Discriminator Retraining

In the current ND280, TPC identifies each track coming from FGD. This can be done when an electron does not cause a shower. On the other hand, SuperFGD has a longer length along the beam axis than FGD. This makes an electron from a ν_eCC event more likely to cause a shower. In such a case, analyzing all the SuperFGD tracks at once and deciding whether the structure is shower-like or not is appropriate.

In this chapter, the electron identification method for selecting electrons using showers in SuperFGD is discussed. Particle discriminators developed in the previous study are retrained for further optimization. The particle gun simulation shown in the previous chapter is used for training the particle discriminator.

5.1 Electromagnetic Shower Reconstruction

To determine whether the object in SuperFGD is a shower or not, the tracks from the shower are collected. The method to collect all the tracks was studied in the previous study. First, the "primary track", which is the first track from the particle's starting point, is selected. The staring point is obtained from the true information. Second, the tracks in contact with the primary track are collected as "connected tracks". The definition of whether the tracks are in contact is that the minimum distance between the two tracks is within 30 mm. Tracks in contact with connected tracks are also considered as connected tracks. Finally, a cone with an opening angle of 30° is constructed. The starting point and direction of the primary track are the tip and axis of the cone. The tracks contained in the cone are collected as "distant tracks". This cone will be used to calculate the discrimination variables for electron identification in the later steps. The reconstruction flow is summarized in Fig. 5.1.
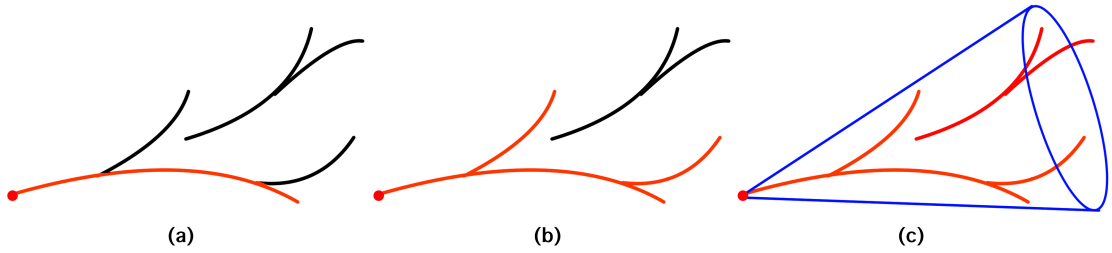
Figure 5.1. The shower reconstruction flow. The red and black lines are tracks from the shower. The red tracks are the selected tracks. (a) The primary track and its starting point is selected. (b) The connected tracks are selected. (c) A cone is constructed and the tracks inside are selected.

5.2 Shower Identification

After collecting the tracks, the next objective is to decide whether the structure is shower-like or not. This is done by calculating the discrimination variables and processing them with a machine learning method called Gradient Boosted Decision Tree (GBDT). The samples are separately processed depending on whether the primary track is contained or escaping SuperFGD. A track is labeled "escaping" when it has a hit in the outermost layer. Escaping tracks are expected to behave differently, affecting the Bragg peak, EM shower and so on. Discriminators were created each for contained and escaping samples to handle these differences.

5.2.1 Update from the Previous Study

In the previous study all of the particle gun data sample was used. However, this sample had electrons that stopped inside or escaped SuperFGD before causing a shower. This is not appropriate since the essential goal is identifying shower-like structures. There is still room for improvement by changing the treatment of the samples. To create a better discriminator, the following "pre-selection" is applied to each sample in this study: The number of connected tracks is two or more, or the number of distant tracks is two or more. This is to ensure that there are at least two tracks from an e^-e^+ pair, meaning there is a gamma produced by bremsstrahlung. This pre-selection is also applied to the muon, pion and proton samples. The events that pass the cut have secondary particles such as delta rays. Table 5.1 shows the number of the particle gun samples that passed the pre-selection, and these were used as training data. However 73% of the escaping electrons do not pass the pre-selection, these will be selected with TPC. The selection using TPC is discussed in Sec. 6.4.

Table 5.1. The number of the particle gun samples which passed the pre-cut and its percentage to the number before the pre-selection.

	electron	muon	pion	proton
contained	496697 (83%)	75648 (33%)	422941 (44%)	136352 (17%)
escaping	340348 (27%)	69405 (4%)	94364 (9%)	19717 (2%)

5.2.2 Discrimination Variables

After the pre-selection, the discrimination variables are calculated. The variables for shower identification is the same as the previous study. There are ten variables which are:

1. The number of connected tracks

2. The number of distant tracks

3. The length of the primary track

4. dE/dx of the primary track

5. The total energy loss in the cone

6. Axis Max Ratio

7. Truncated Max Ratio

8. Q Root Mean Square

9. Front Back Ratio

10. Maximum Hit Position.

The distribution for each particle of the first five are shown in Fig. 5.2 and Fig. 5.3. The definition of the last five are as follows.

Axis Max Ratio

Axis Max Ratio (AMR) shows how wide the hits are distributed. AMR is the "cone width" divided by the "cone depth". The cone width is defined as the distance between the cone axis and the farthest hit from it. The cone depth is defined as the distance between the cone tip and the farthest hit from it. AMR is written as

$$\text{AMR} = \frac{\text{cone radius}}{\text{cone depth}}. \tag{5.1}$$

AMR will be large for electrons due to their large cone radius from the shower. Protons and pions stop or decay early which makes their cone depth small. Because of it, AMR will be much larger. The distribution for each particle gun sample is shown in Fig. 5.4.

Truncated Max Ratio

Truncated Max Ratio (TMR) shows how the energy loss varies. The cone is sliced along its axis for every 50 mm and the hit charge is summed for each slice. TMR is the charge ratio between the minimum and maximum charged slice. It is written as

$$\text{TMR} = \frac{\text{charge in the minimum charged slice}}{\text{charge in the maximum charged slice}}. \tag{5.2}$$

TMR will be large for muons because their energy loss does not change so much. The distribution for each particle gun sample is shown in Fig. 5.5.

Q Root Mean Square

Q Root Mean Square (QRMS) is the standard deviation of the hit charge divided by the mean hit charge. It is expressed as

$$\text{QRMS} = \frac{1}{\bar{q}} \sqrt{\sum_i^N \frac{(q_i - \bar{q})^2}{N}} \tag{5.3}$$

where N is the number of the hits, q_i is the charge of each hit and $\bar{q}$ is the mean hit charge. The distribution for each particle gun sample is shown in Fig. 5.6.

Front Back Ratio

Front Back Ratio (FBR) is similar to TMR. However this time the cone is sliced in to quarters along its axis. FBR is the charge ratio between the slice at the tip and the bottom of the cone. It is written as

$$\text{FBR} = \frac{\text{charge in the bottom slice}}{\text{charge in the tip slice}}. \tag{5.4}$$

The distribution for each particle gun sample is shown in Fig. 5.7.

Maximum Hit Position

Maximum Hit Position (MHP) is the distance between the cone tip and the most energetic hit. It is normalized by dividing with the cone depth. Particles with Bragg peak will have MHP close to 1. The distribution for each particle gun sample is shown in Fig. 5.8.
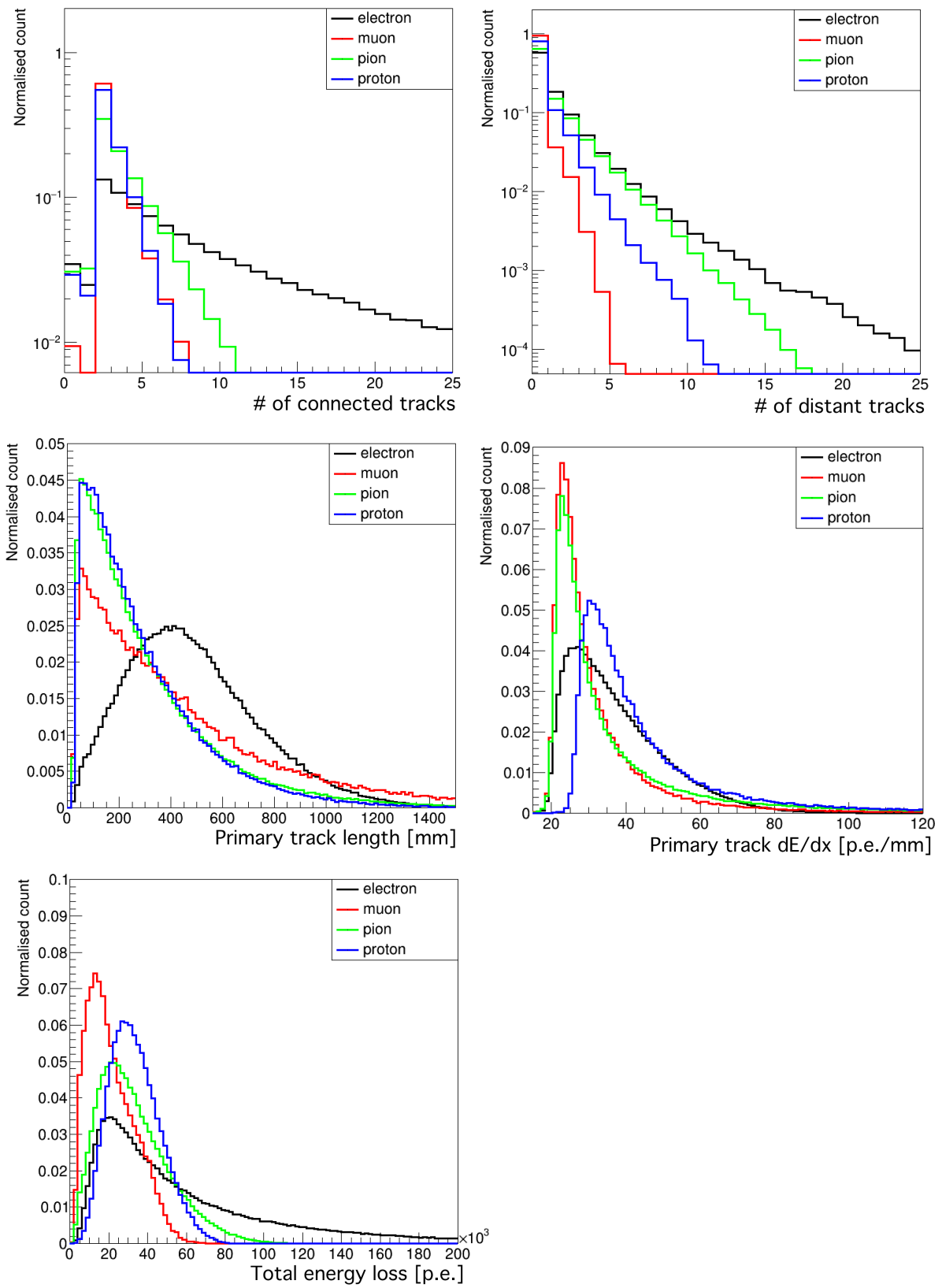
Figure 5.2. The distribution of discrimination variables for contained samples. The unit p.e. is the number of photo-electrons.
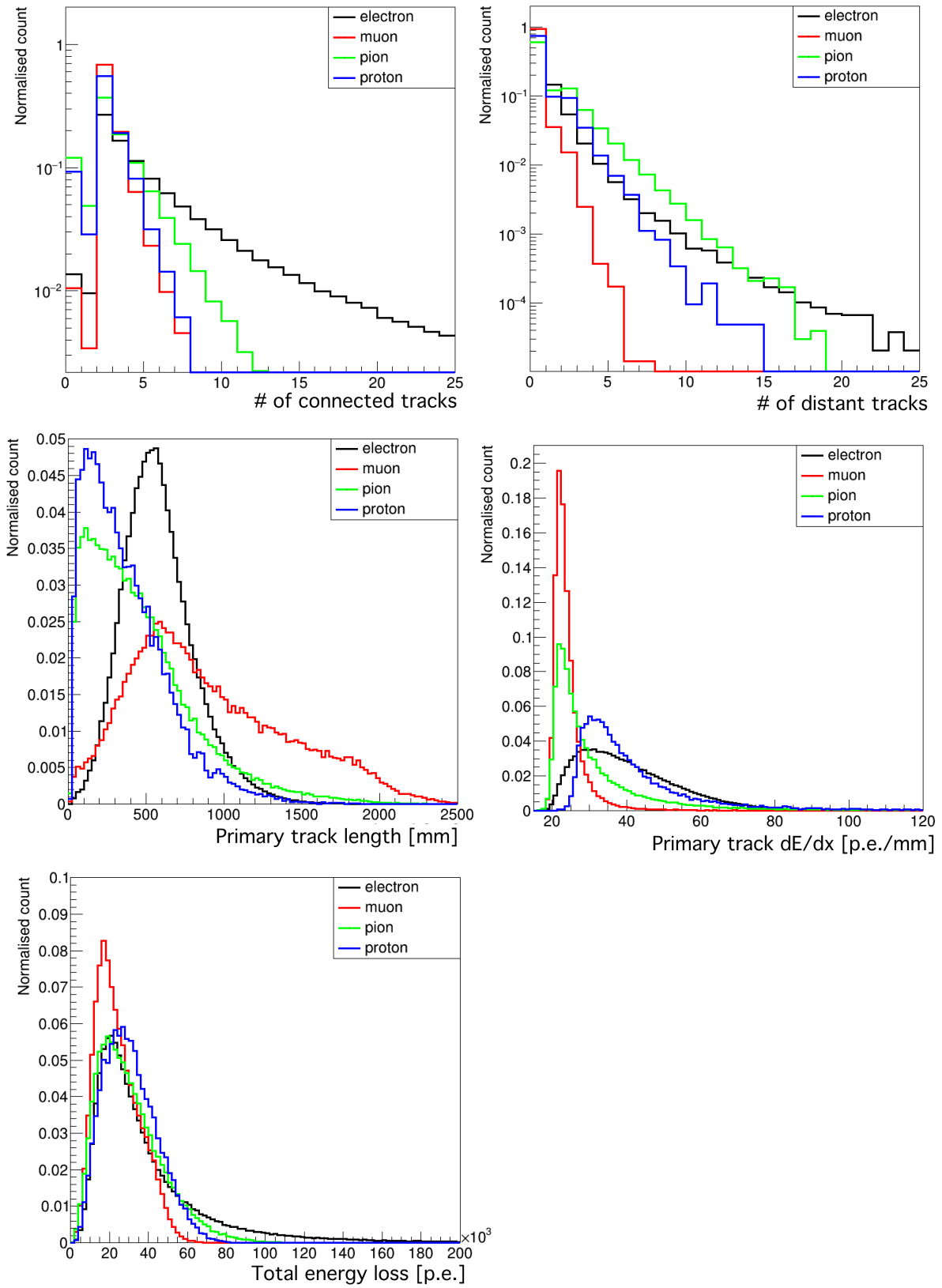
Figure 5.3. The distribution of discrimination variables for escaping samples. The unit p.e. is the number of photo-electrons.
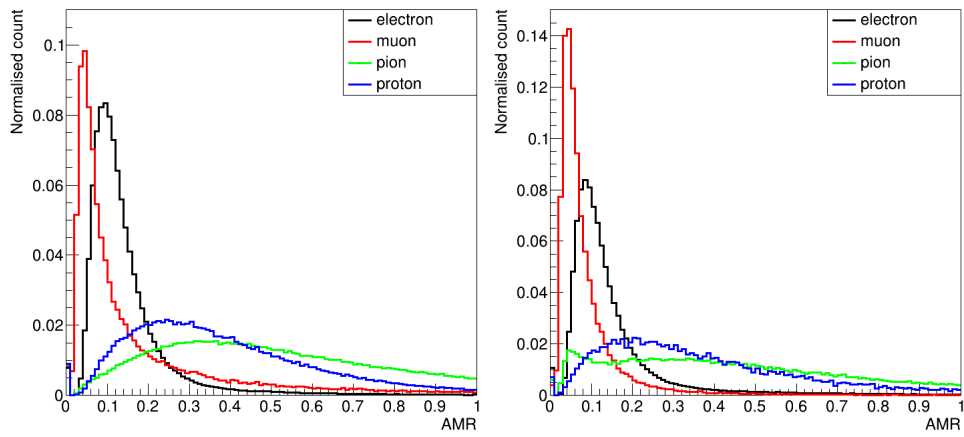
Figure 5.4. The distribution of AMR for contained (left) and escaping (right) samples.
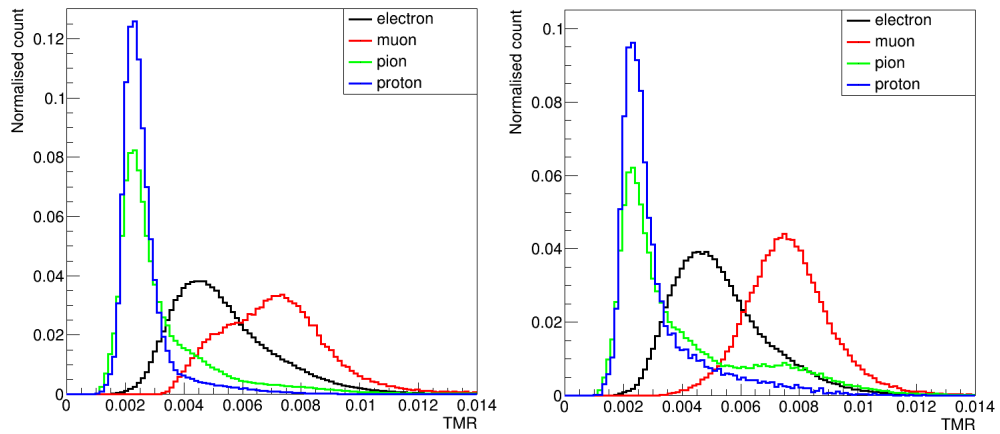
Figure 5.5. The distribution of TMR for contained (left) and escaping (right) samples.
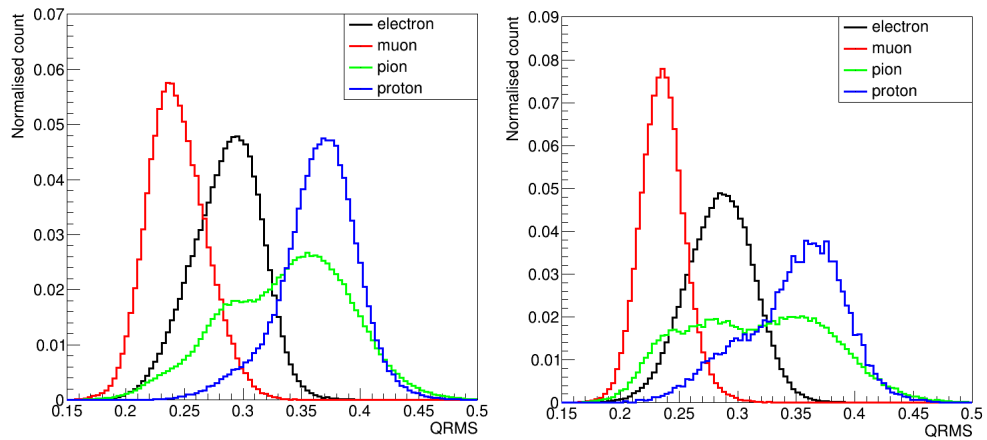
Figure 5.6. The distribution of QRMS for contained (left) and escaping (right) samples.
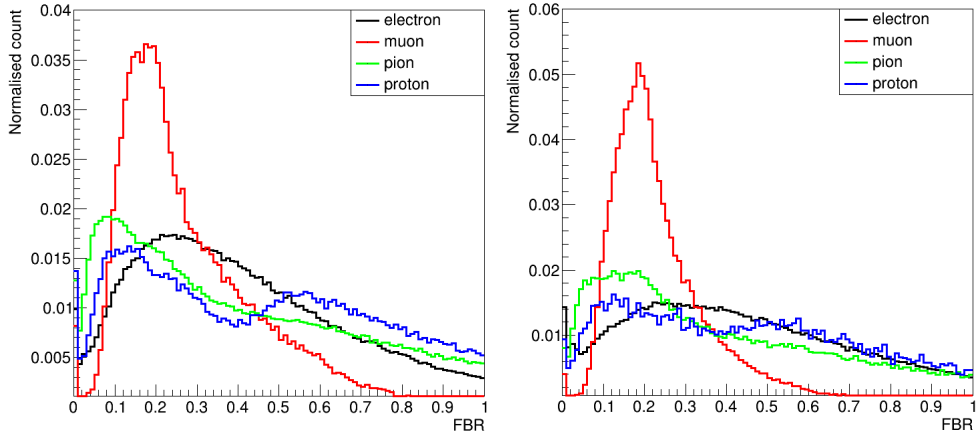
Figure 5.7. The distribution of FBR for contained (left) and escaping (right) samples.
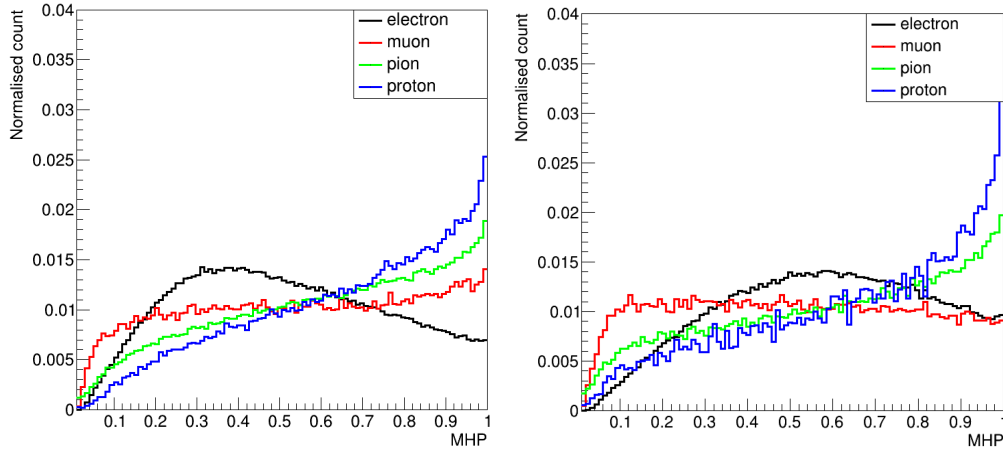
Figure 5.8. The distribution of MHP for contained (left) and escaping (right) samples.

5.2.3 Classification Result

With the discrimination variables calculated, particle discriminators are trained for e^-/μ^-, e^-/π^+ and e^-/p separation, each for contained and escaping samples. GBDT is used for these discriminators. Besides GBDT, there are various methods for classifying data such as the k-nearest neighbor method (kNN), Fisher's linear discriminant and the maximum likelihood method. However, these methods are less efficient compared to GBDT in this study. The output for each discriminator using GBDT and its ROC curve is shown in Fig. 5.9, 5.10, 5.11, 5.12, 5.13 and 5.14. The ROC curves include results using other methods besides GBDT. Also, the ROC curves for the discriminators in the previous study are compared with the same sample after the pre-selection (Fig. 5.15, Fig. 5.16 and Fig. 5.17). The performance improved especially for escaping samples.

To decide whether the event is electron-like or not, the discriminator threshold must be set. The optimization of the threshold is discussed in Sec. 6.4. Samples that pass all

three discriminators are considered electron-like. Table 5.2 is an example of the selection efficiency with all the thresholds at 0.9. With this selection, the electron efficiency is 70% for contained samples and 63% for escaping samples, and the background efficiency is around 1% or less.

Table 5.2. Efficency of the particle gun samples which passed the all the discriminators with all the thresholds set at 0.9.

	electron	muon	pion	proton
contained	70.4%	1.2%	0.5%	0.1%
escaping	63.1%	0.9%	0.2%	0.2%
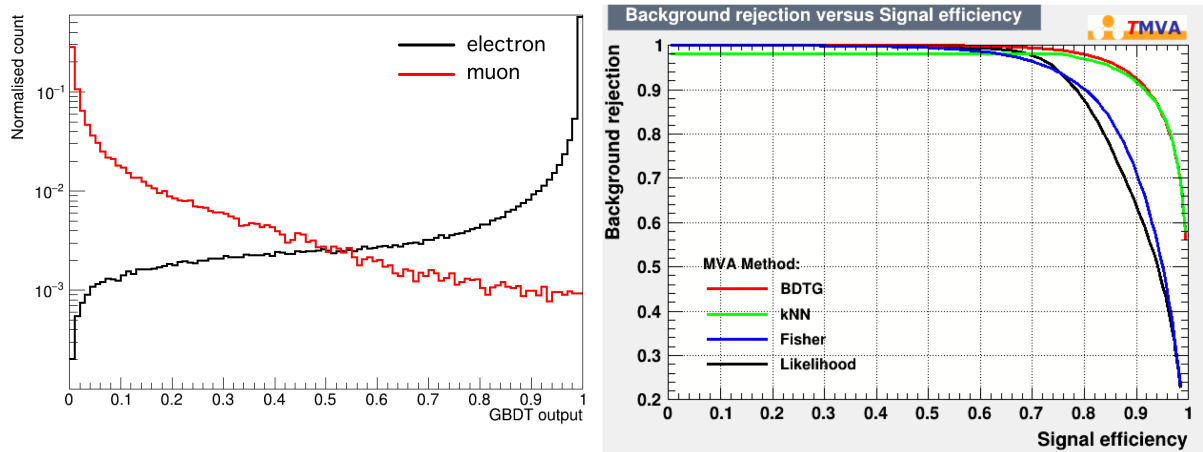
Figure 5.9. The contained e^-/μ^- discriminator output (left) and ROC curve (right).
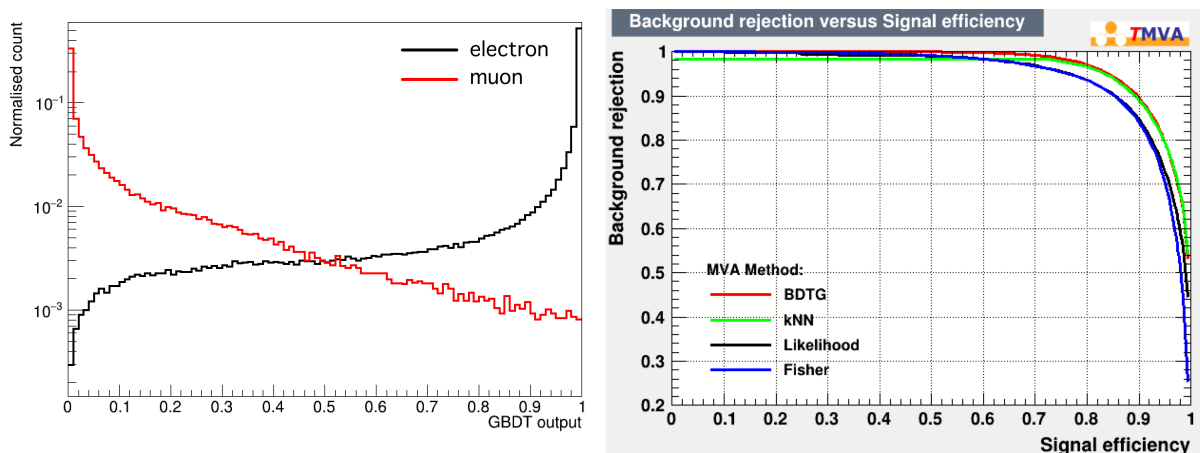
Figure 5.10. The escaping e^-/μ^- discriminator output (left) and ROC curve (right).
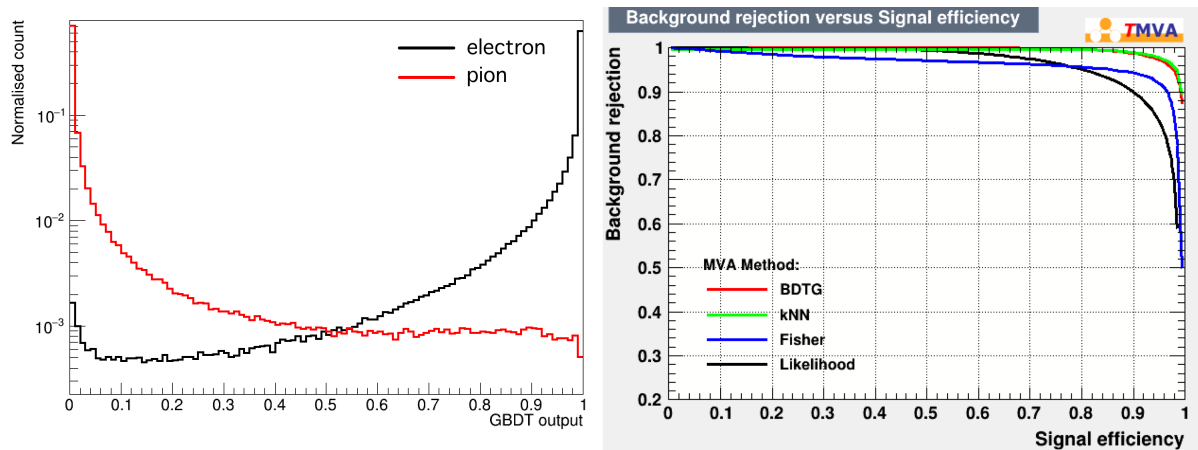
Figure 5.11. The contained e^-/π^+ discriminator output (left) and ROC curve (right).
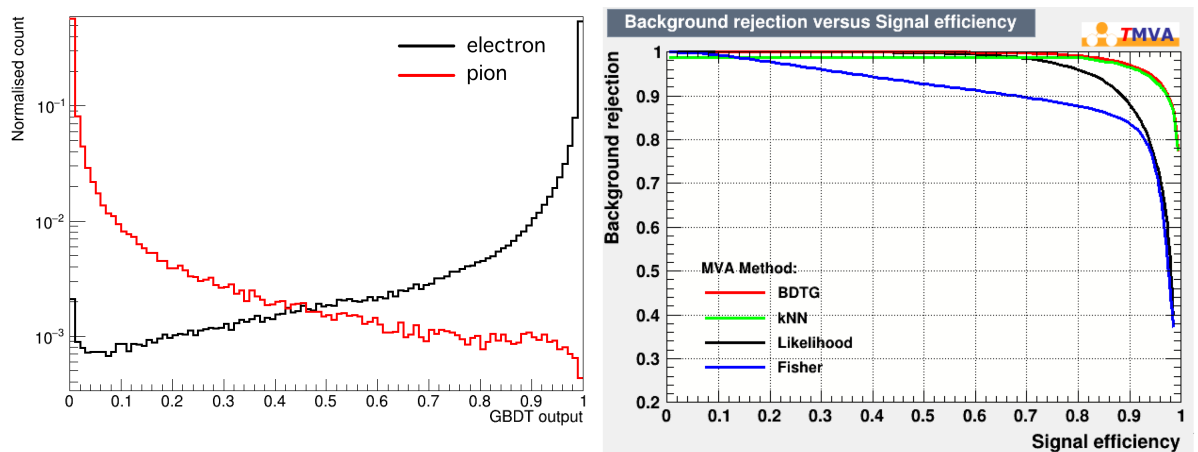
Figure 5.12. The escaping e^-/π^+ discriminator output (left) and ROC curve (right).
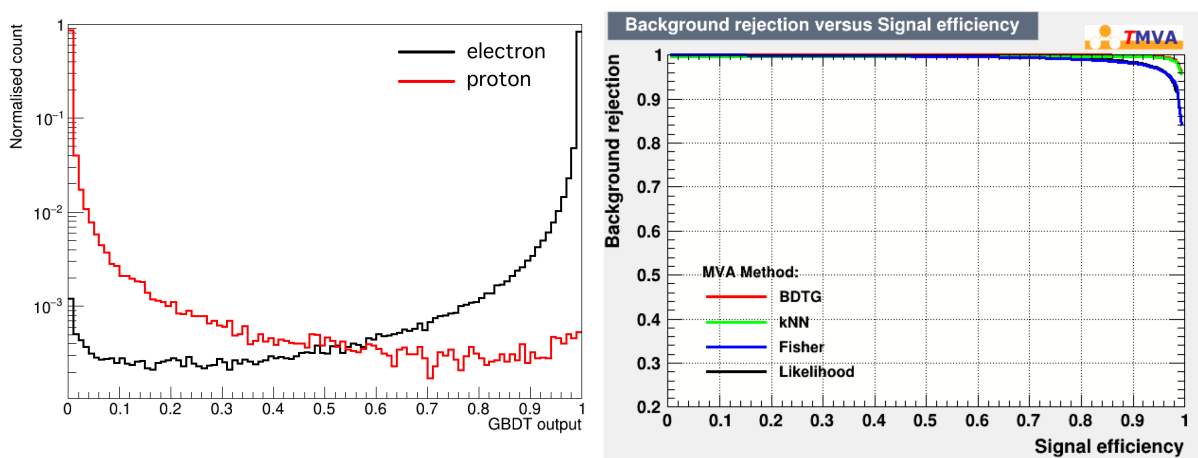
Figure 5.13. The contained e^-/p discriminator output (left) and ROC curve (right).

43
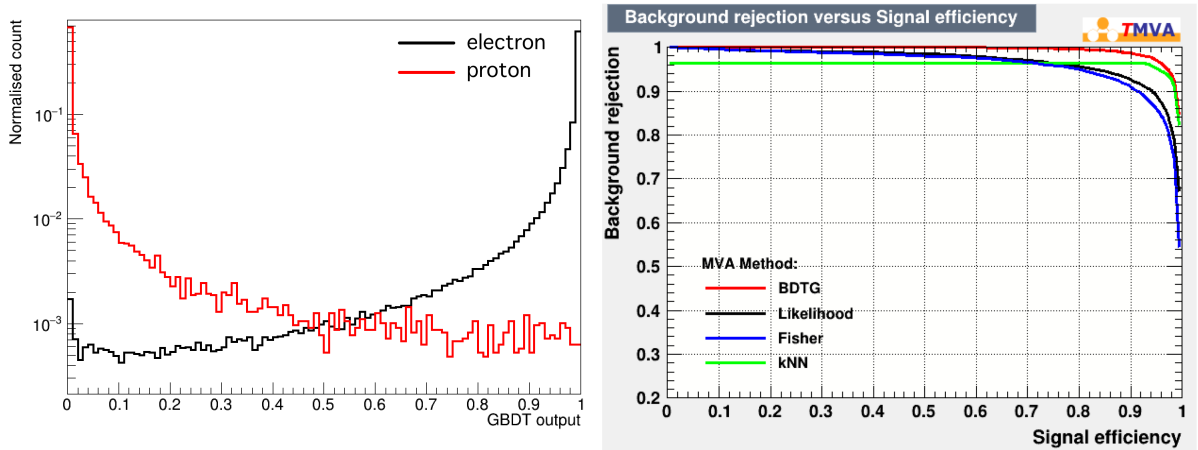
Figure 5.14. The escaping e^-/p discriminator output (left) and ROC curve (right).
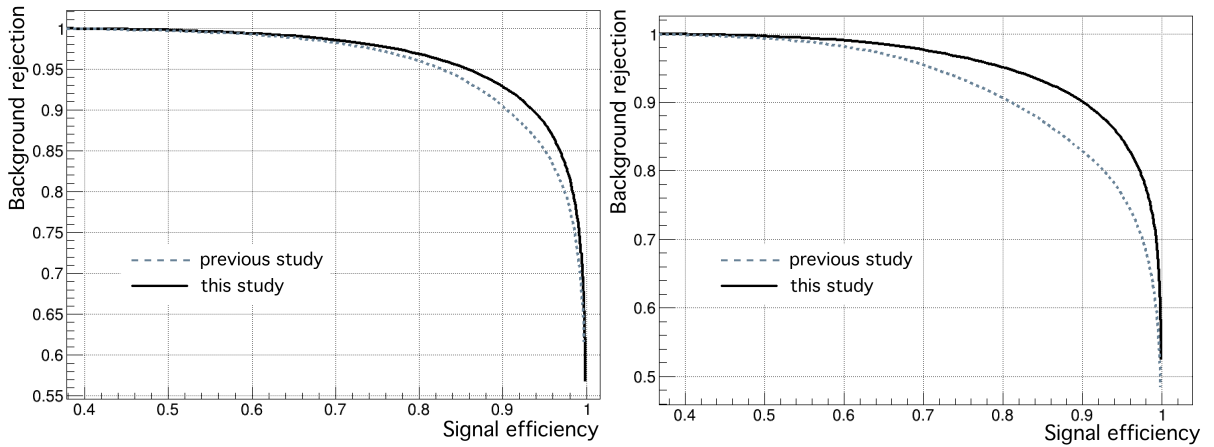
Figure 5.15. ROC curve of the e^-/μ^- discriminator created in the previous study and this study. The left figure is for contained samples and the right is for escaping samples.
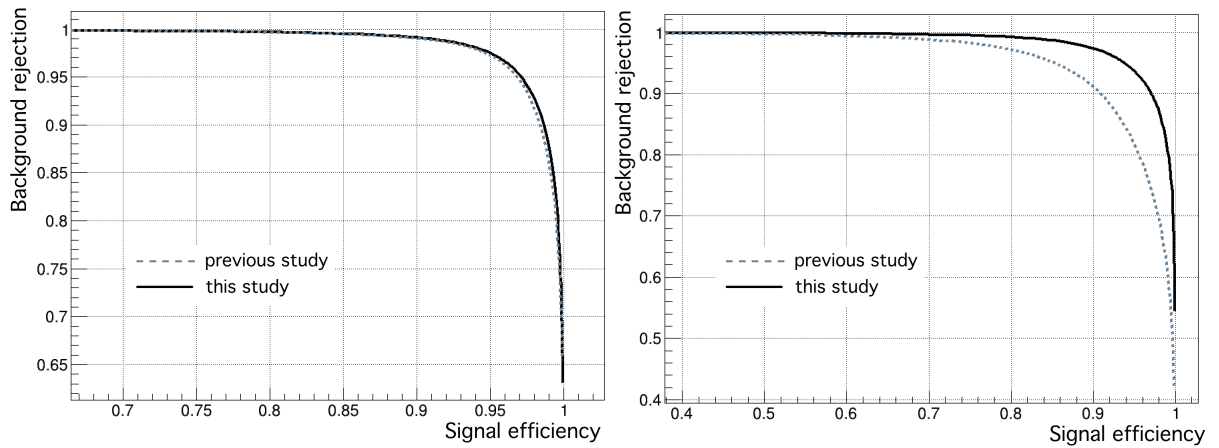
Figure 5.16. ROC curve of the e^-/π^+ discriminator created in the previous study and this study. The left figure is for contained samples and the right is for escaping samples.
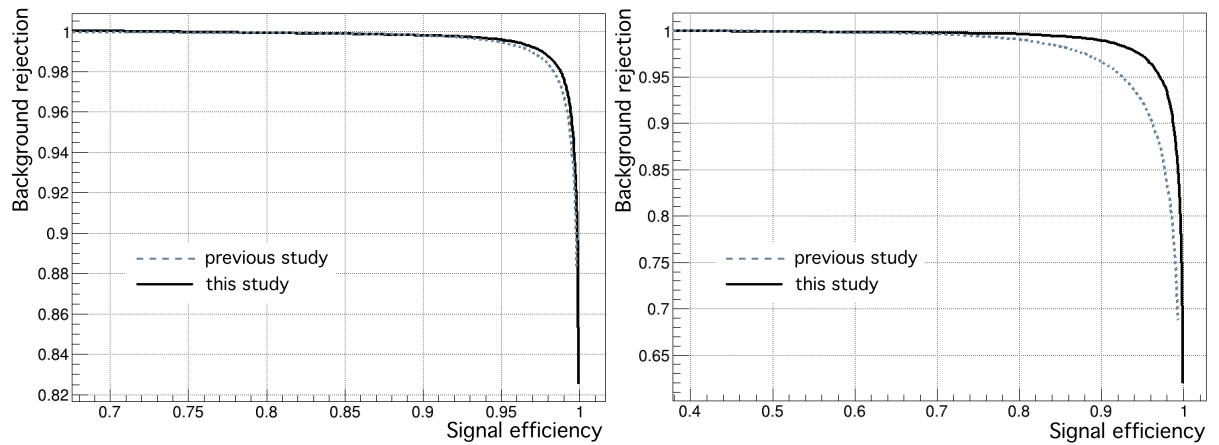
Figure 5.17. ROC curve of the e^-/p discriminator created in the previous study and this study. The left figure is for contained samples and the right is for escaping samples.

Chapter 6

Electron Neutrino Selection

In this chapter, the ν_eCC event selection is discussed. The neutrino interaction sample explained in Sec. 4.1 is used for this study. As explained in Sec. 3.6, the previous study used neutrino events where the produced leptons stop in SuperFGD, and only the information from SuperFGD was analyzed. In this study, information from TPC, HAT and ECal are also used to select escaping electrons. The selection performance using HAT is estimated from that of TPC because the reconstruction of HAT is not yet developed.

The summary of the selection flow is shown in Fig. 6.1. To optimize each selection step, the figure of merit (FM) is defined as the product of the efficiency and purity of ν_eCC events. The selection is considered better when the FM is larger.
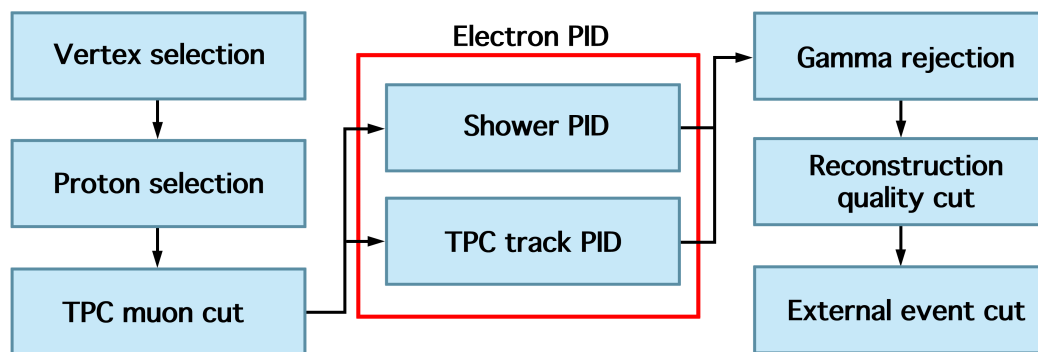
Figure 6.1. The summary of the ν_e CC event selection.

6.1 Vertex Selection

Since the neutrino beam is spread out and is not concentrated at a single point, neutrinos can interact at any position in SuperFGD. To analyze each neutrino event, the interaction vertex must be selected first. For ν_μ events, it is simply selected by finding the starting point of a muon-like track. However, this cannot be applied to ν_e events because an EM shower occurs and there are multiple tracks from the primary electron track. There is a different algorithm for vertex selection in ν_e events. First, the vertices in the middle of the track are rejected. Second, the direction of tracks with lengths longer than 30 cm are checked, and the vertices that do not agree with those directions are rejected. SuperFGD has a time resolution better than 1 ns and is capable of determining the track direction longer than 30 cm. Third, the vertices that are more than 2 ns later than the first hit timing in SuperFGD are rejected. This is done to cut isolated tracks. Finally, the vertex which is connected to the longest track is selected as the interaction vertex. Vertices are selected in 99% of the ν_e or ν_μ CC events in SuperFGD. Figure 6.2 shows the distance between the selected and true vertex for CC events in SuperFGD. For 85% of the events, the distance is less than 30 mm.

Also, there are cases where the vertex is selected inside SuperFGD while the actual interaction vertex is outside SuperFGD. If there is a charged particle entering SuperFGD, the vertex at the entering point should be selected. Events where the selected vertices are outside the SuperFGD FV are rejected to cut such cases. However, if a gamma enters and converts inside SuperFGD, the selected vertex will be inside the SuperFGD FV and cannot be rejected. These events will be dealt with in the later steps.
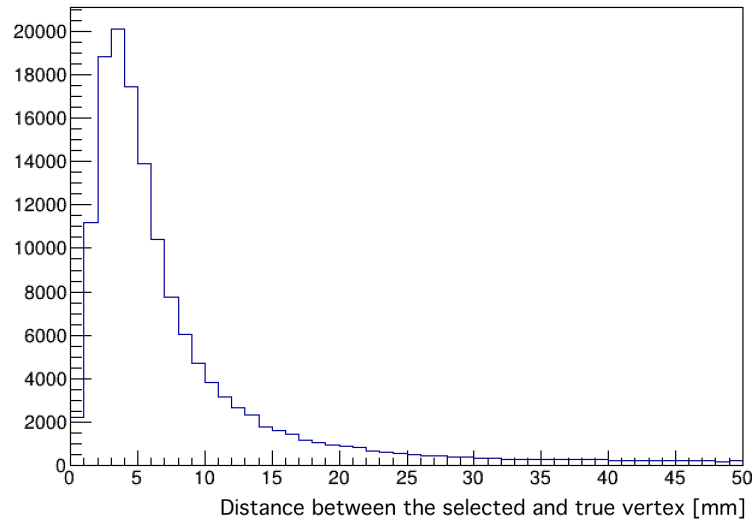
Figure 6.2. The distance between the selected and true vertex for CC events in Super-FGD.

6.2 Proton Selection

Tracks within 30 mm from the selected vertex are considered primary tracks. Before finding electrons, first the Bragg peaks of protons are searched. This is done by checking the maximum hit charge of the primary tracks. Since gamma conversion does not produce protons, rejecting events without Bragg peaks can cut the gamma background from outside. This can also cut antineutrino CCQE background which is $\nu_l + p \rightarrow l^+ + n$. Figure 6.3 and Figure 6.4 show the maximum hit charge in events with one primary track and two or more primary tracks, respectively. Figure 6.5 shows the FM as a function of the threshold of the maximum hit charge for events with one primary track. The peak is at around 400 photo-electrons (p.e.) to 800 p.e. Figure 6.6 shows the FM for events with two or more primary tracks and the peak is at 0 to 500 p.e. The threshold is set at 800 p.e. for events with one primary track and 500 p.e. for events with two or more primary tracks to reject background events as much as possible.
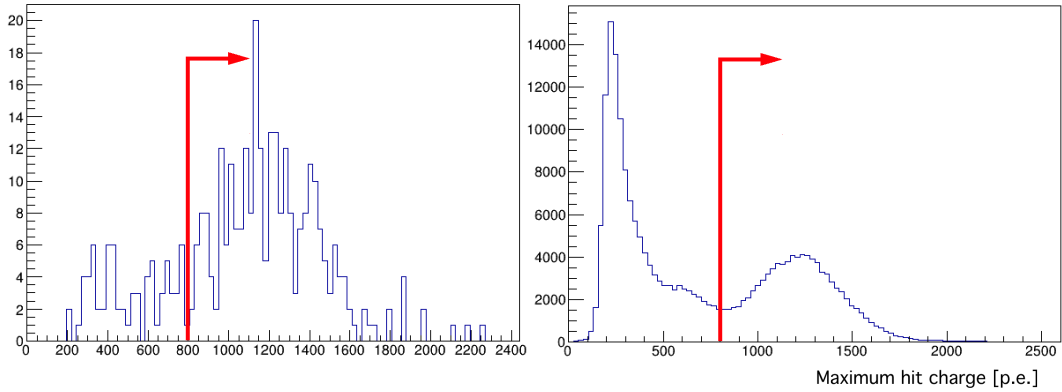
Figure 6.3. The maximum hit charge in ν_eCC events (left) and background events (right) with one primary track.
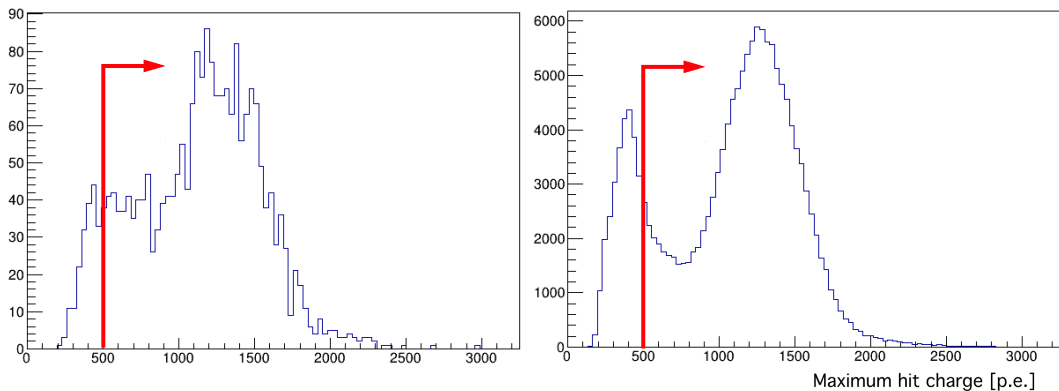
Figure 6.4. The maximum hit charge in ν_eCC events (left) and background events (right) with two or more primary tracks.
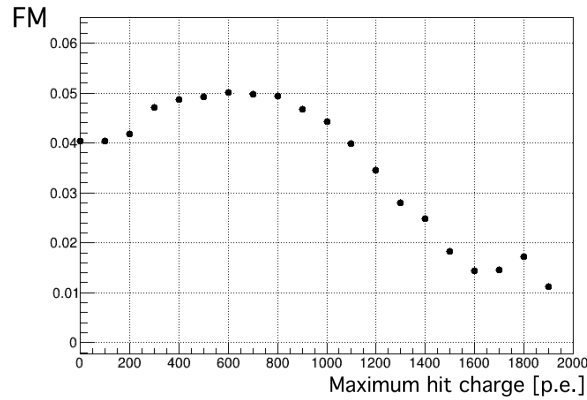
Figure 6.5. The FM as a function of the maximum hit charge threshold in events with one primary track.
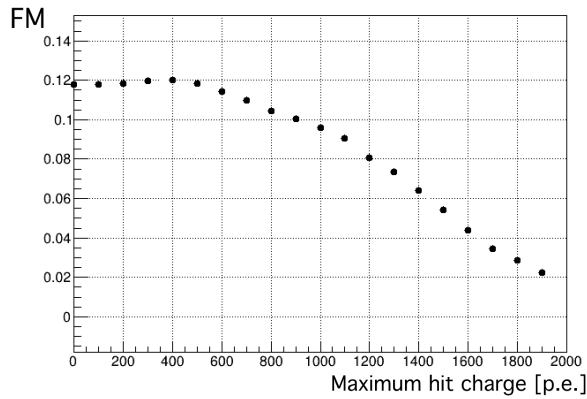
Figure 6.6. The FM as a function of the maximum hit charge threshold in events with two or more primary track.

6.3 TPC Muon Cut

To check that the event is not a ν_μCC event, the track with the largest momentum in TPC is checked whether it is muon-like or not. If it is muon-like, the event is rejected. Tracks with less than 20 hits are not checked in this cut. This is because the average muon momentum is 600 MeV/c which corresponds to curvature radius 10 m in TPC and it must travel 14 cm so that the curve can be detected. This corresponds to approximately 20 hits. Also, tracks with momentum less than 300 MeV/c are not checked since muons with momentum less than 300 MeV/c quickly lose their energy and it is difficult to measure the momentum in that region (Fig. 6.7). Figure 6.8 is the FM as a function of the threshold of the muon likelihood. The peak is at around 0.05 to 0.2 and the threshold is set at 0.05 to maximize the background rejection.

49
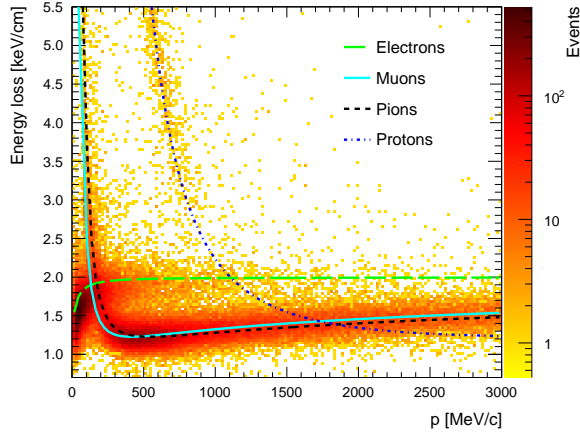
Figure 6.7. The momentum and energy loss measured in TPC [9]. Each line shows the predicted energy loss.
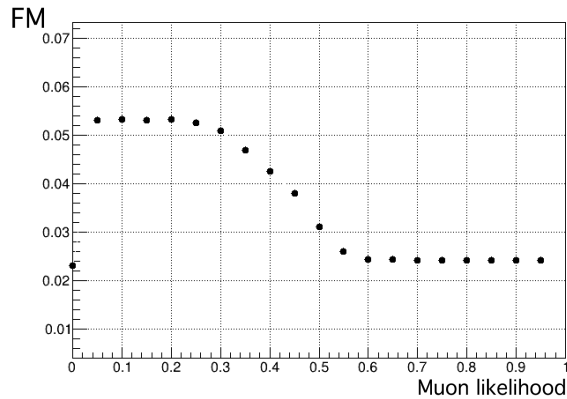
Figure 6.8. The FM as a function of the muon likelihood threshold.

6.4 Electron PID

To find electrons, two types of PID are applied which are shower PID and TPC track PID. First the shower PID is applied to each primary track. Figure 6.9 shows the FM with various thresholds for the e/μ and e/π discriminators, with the e/p threshold set at 0.5. The best threshold is $(e/\mu, e/\pi) = (0.80, 0.95)$. With these e/μ and e/π thresholds, changing the e/p threshold does not affect the selection so the threshold is set at $(e/\mu, e/\pi, e/p) = (0.80, 0.95, 0.5)$.

If the event does not pass the shower PID, the TPC track PID is applied. The same selection flow used in [9] is used. First, tracks in TPC that start from the interaction vertex are selected. Second, the track with the largest momentum is selected. This track is called the "leading track" and this must be negatively charged. Finally, the PID in TPC and ECal are applied, and is decided whether it is an electron or not. Same as the muon

50

PID cut, the selection requires that the leading track has enough hits. The threshold is set at 26 hits since the average electron momentum is around 1 GeV/c and TPC needs 26 hits to measure the curvature at that momentum. As shown in Fig. 6.7, the energy loss of a muon and an electron at momentum 150 MeV/c is the same. Tracks with momentum less than 200 MeV/c are not checked to avoid muon contamination. Figure 6.10 shows the electron likelihood and reconstructed momentum of the leading track in TPC. The electron likelihood threshold is set at 0.96 since there are few signals in the region below 0.96. ECal PID is applied when the track enters ECal. Figure 6.11 shows the ECal PID output $R_{\mathrm{MIP/EM}}$, and the threshold is set at 0.
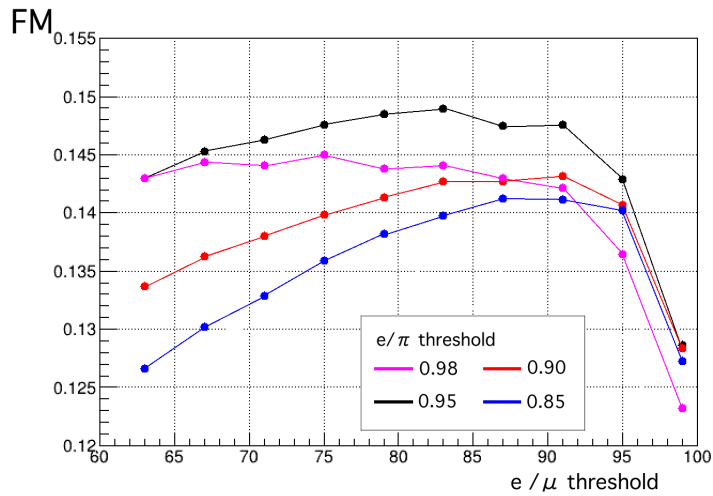
Figure 6.9. The FM as a function of the e/μ discriminator threshold with the e/p threshold set at 0.5.
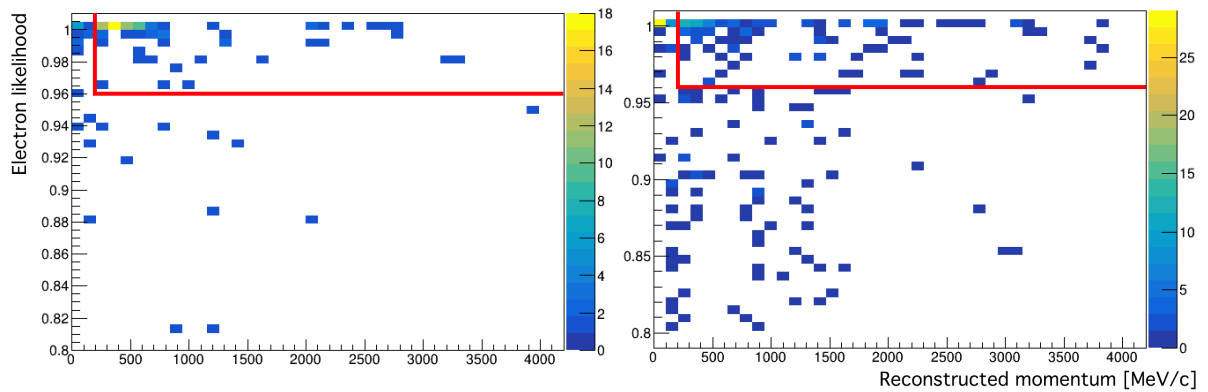
Figure 6.10. The electron likelihood of the most energetic track in TPC for ν_eCC events (left) and background events (right).

51
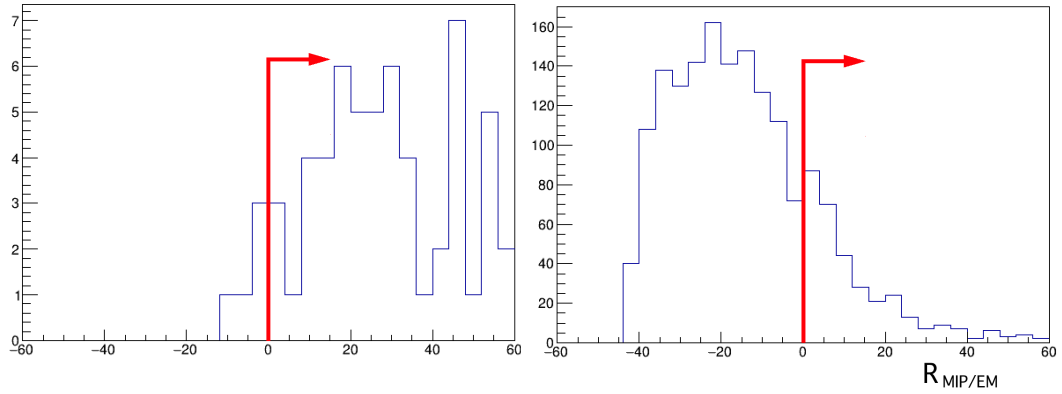
Figure 6.11. The ECal PID output for ν_eCC events (left) and background events (right).

6.5 Gamma Rejection

After selecting an electron, the next step is to check that the electron was produced from a ν_eCC interaction and not from gamma conversion. In this cut, the electron/gamma discriminator developed in the previous study is used. This discriminator checks the energy loss at the starting point of the shower. A shower from a gamma has an e^-e^+ overlap at the starting point which makes the energy loss two times larger than a single electron. The e/γ discriminator output is shown in Fig. 6.12. The FM as a function of the e/γ threshold is shown in Fig. 6.13. The threshold is set at 0.2 since the peak is at 0.2.
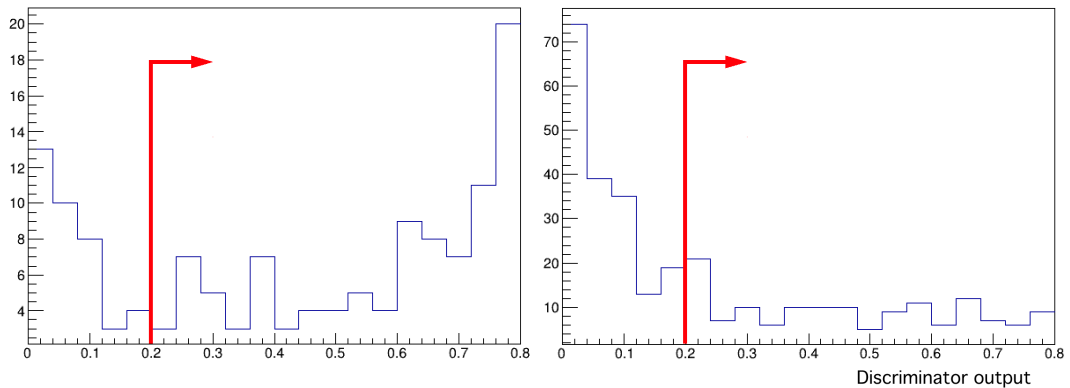
Figure 6.12. The e/γ discriminator output for ν_eCC events (left) and background events (right).
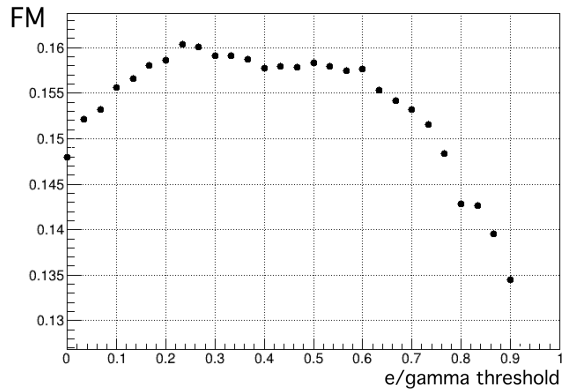
Figure 6.13. The FM as a function of the e/γ discriminator threshold.

6.6 Reconstruction Quality Cut

When multiple particles are emitted in the same direction from the interaction vertex, tracks are concentrated around the starting point. This makes it difficult to correctly reconstruct tracks. Figure 6.14 shows an example of an event where the reconstruction is not accurate. In such cases, some primary tracks can be reconstructed far from the vertex, and they will be processed as connected tracks. The output of the EM shower discriminator cannot be relied on in these events. Figure 6.15 shows the distance between the vertex and the nearest connected track. The FM is shown in Fig. 6.16 and the peak is at 35 mm. In this study, the threshold is set at 35 mm.
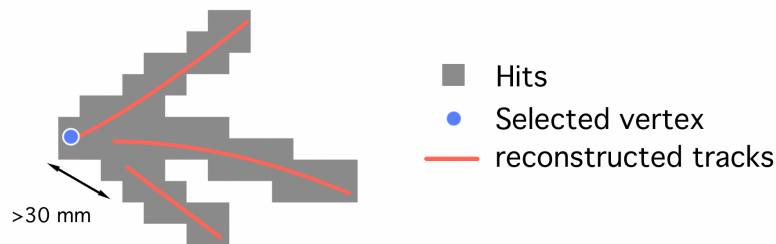
Figure 6.14. A case where the reconstruction is not accurate. A track is reconstructed 30 mm away from the selected vertex.
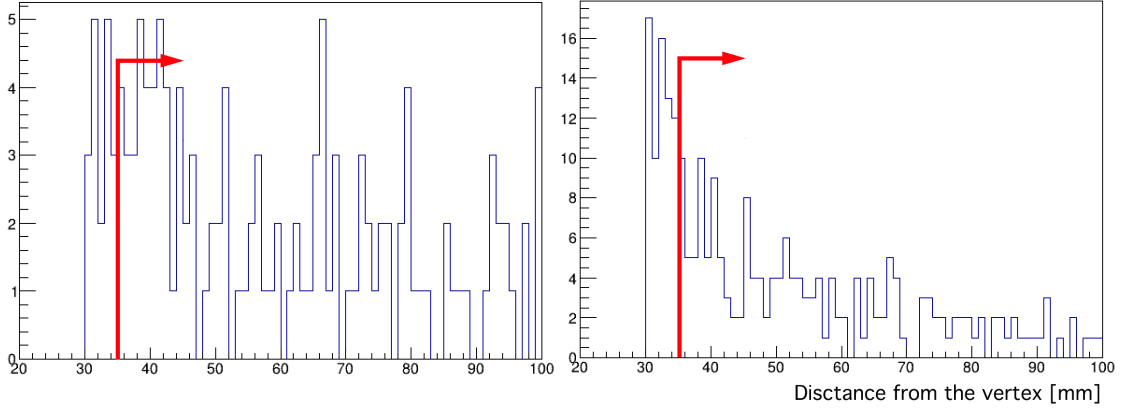
Figure 6.15. The distance between the selected vertex and the nearest connected track for ν_eCC events (left) and background events (right).
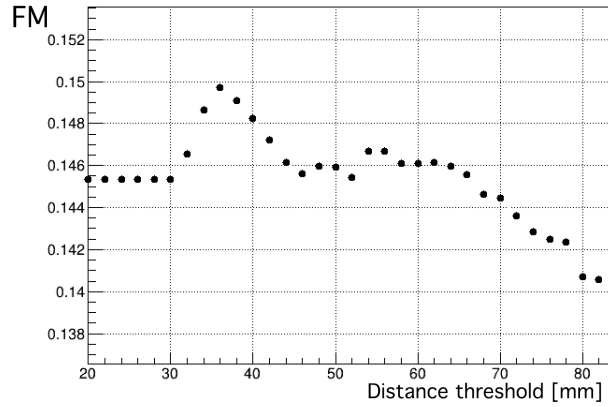
Figure 6.16. The FM as a function of the distance between the selected vertex and the nearest connected track.

6.7   External Event Cut

Among the selected events, almost all of the external background events are from Us-ECal and the upstream part of the magnet (Fig. 6.17). The typical time of flight between Us-ECal and SuperFGD is less than 1 ns. The timing information of Us-ECal cannot be used for cutting external events because its resolution is around 7 ns. For this study, events that have a reconstructed object in Us-ECal are rejected as external events. Table 6.1 summarizes this cut, and about 40% of the external events are rejected.
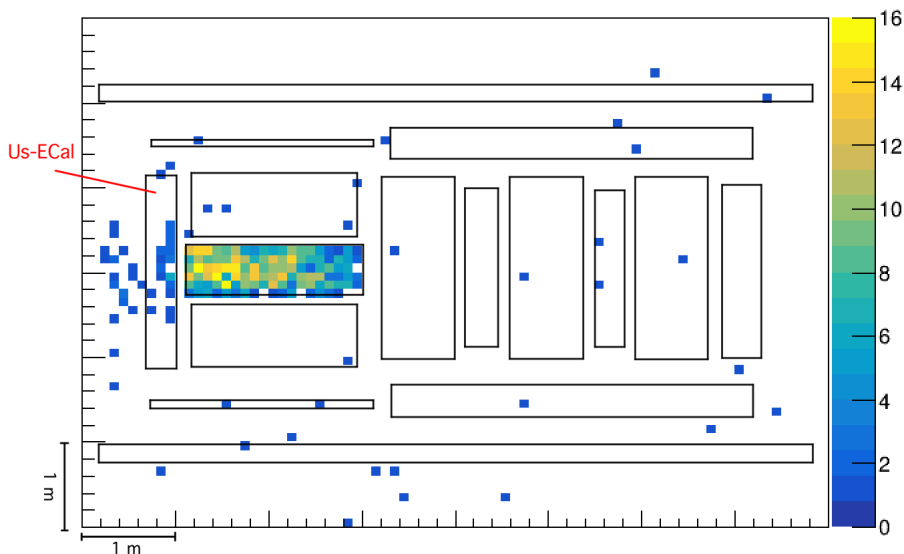
Figure 6.17. The side view of the true vertex position.

Table 6.1. The position of the actual vertex and the number of events, before and after the cut.

	SuperFGD	Magnet	Us-ECal	Other
Before	873	46	32	12
After	855	23	17	11

6.8　Selection Result

Currently, the reconstruction of HAT is not available. However, the selection performance of HAT can be estimated from that of TPC. In this study, the performance is estimated by assuming that it is the same as the selection performance for CC events with the following conditions: The leptons escape to TPC and the true vertex position is within 56 cm from the downstream surface of SuperFGD. The threshold of 56 cm is the same as the vertical width of SuperFGD.

The number of events after each cut is summarized in Table 6.2. Also, the efficiency and purity at each step are summarized in Fig. 6.18. For the final result, the efficiency and purity of ν_eCC events are 23% and 69%, respectively. The denominator of the efficiency is the number of ν_e events before the selection which is 2701. The true momentum of the selected primary track is shown in Fig. 6.19. The dominant background is ν_μCC events in SuperFGD.

As shown in Table 6.2, there is a large efficiency decrease at the electron PID. The events that did not pass the electron PID are classified in Table 6.3. About half of the rejected ν_e events have showers but did not pass the shower PID. In these events, the shower is small because a large fraction of the shower is not contained in SuperFGD.

The remaining background events can be classified into two cases. The first case is events where $\gamma \rightarrow e^- e^+$ occurred near the vertex. Figure 6.20 shows an example of such an event. The second case is events where a gamma shower occurred near a primary track, making a shower-like structure coming out from the vertex. 80% of the background events in SuperFGD are this second case. As explained in Sec. 5.1, a cone is created for each primary track and tracks inside the cone are collected. This method can end up collecting unrelated tracks. Figure 6.21 shows an example of such an event. The main gamma source is π^0 which is produced in events such as resonance and deep inelastic scattering events.

Table 6.2. The number of events which passed each cut.

	ν_eCC	$\bar{\nu}_e$CC	ν_μCC	$\bar{\nu}_\mu$CC	NC	External
No cut	2701	259	156397	4918	51717	3216686
Vertex selection	2592	239	139032	4476	36146	184362
Proton selection	2342	139	124131	1937	26253	65474
TPC muon cut	2007	124	59566	426	24490	61329
Electron PID	685	42	237	5	96	180
Gamma rejection	638	42	180	2	56	121
Reconstruction quality cut	626	37	163	2	45	90
External event cut	622	33	156	2	42	51
Efficiency	23%	13%	0.1%	0.04%	0.08%	0.001%
Fraction	69%	4%	17%	0.2%	5%	6%

Table 6.3. The events that did not pass the electron PID.

Event type	Ratio
There was a shower, but did not pass the shower PID.	49%
The electron did not have enough hits in TPC.	9%
The electron did not pass the TPC PID.	17%
The electron did not enter TPC.	25%
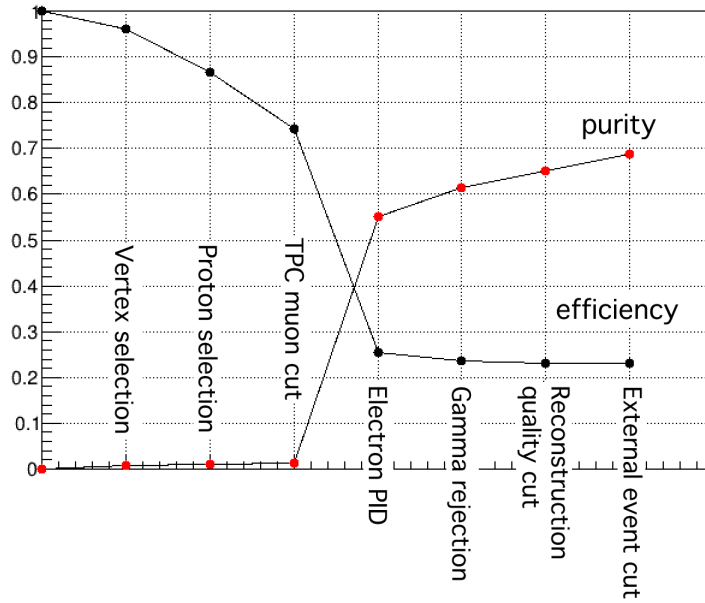
Figure 6.18. The ν_e selection efficiency and purity at each step.
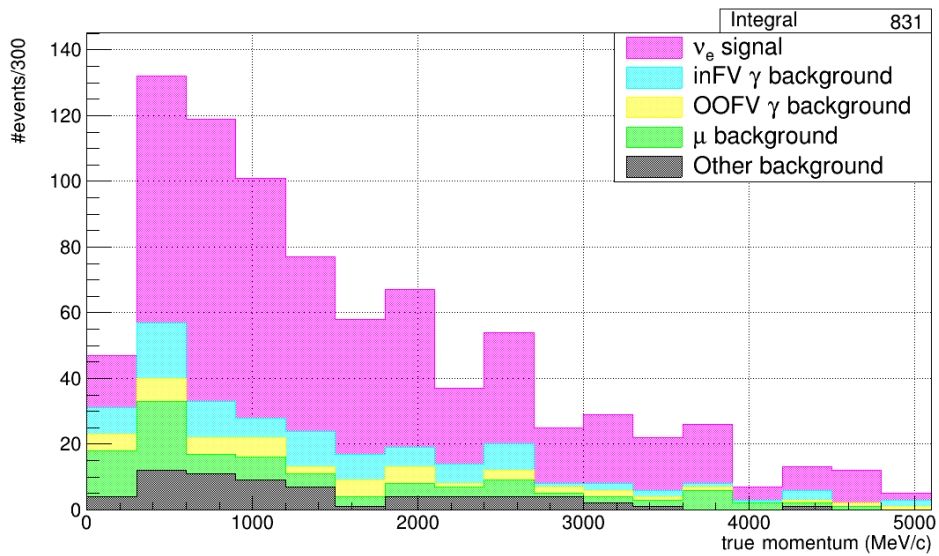
Figure 6.19. The true momentum distribution of the selected primary tracks.
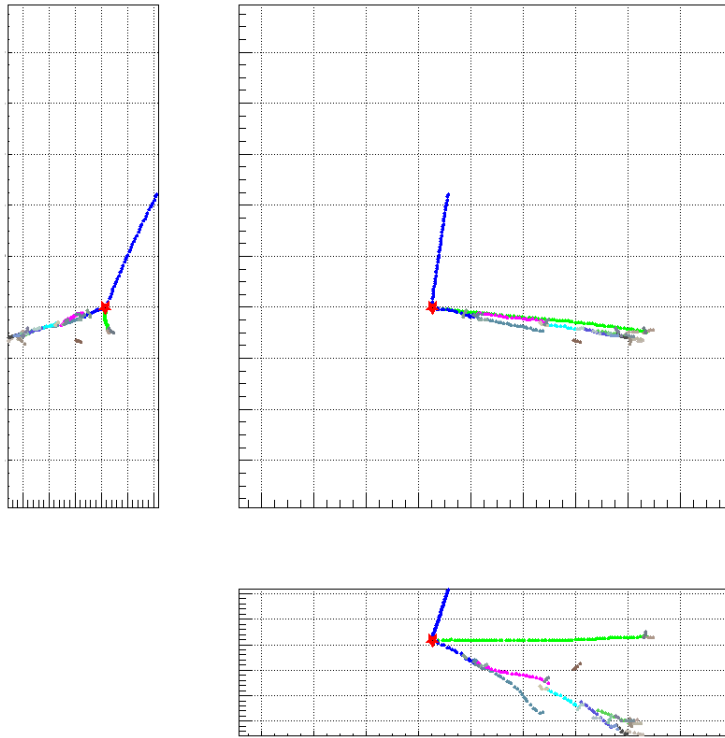
Figure 6.20. A ν_μ CC background that was selected. The red star is the interaction vertex. There is a shower coming out from the vertex but the shower is actually from a gamma.
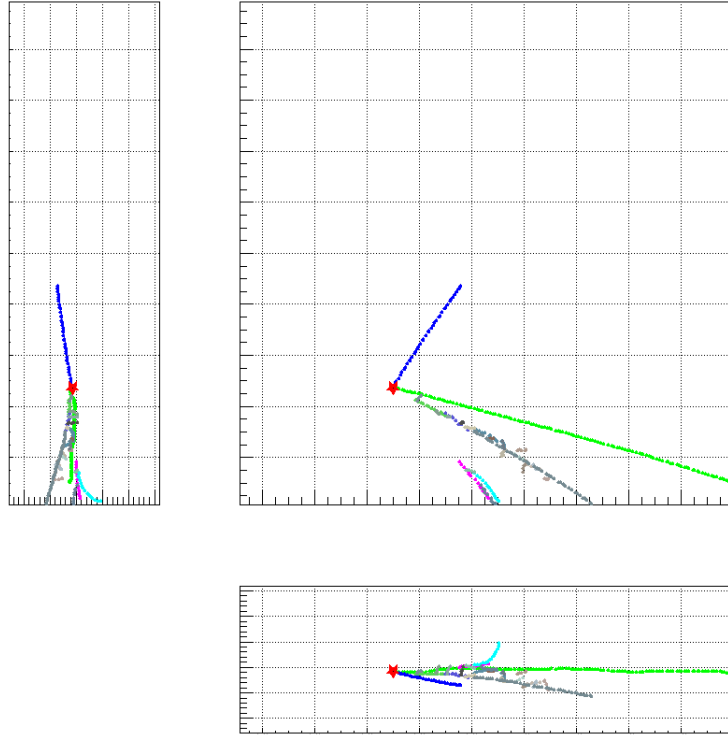
Figure 6.21. A ν_μ CC background that was selected. The red star is the interaction vertex. There is a gamma shower near by a primary track.

Chapter 7

Discussion

7.1 Expected Impact on T2K Experiment

With the method in this study, the upgraded ND280 is capable of selecting ν_eCC events with an efficiency of 23% and purity of 69%. In comparison, the efficiency and purity using the current ND280 is 26% and 54%, respectively. The purity has improved after the upgrade. Although the efficiency has slightly dropped, the absolute event number will be improved since the target mass is twice as large as the current one.

In this study, it is estimated that 622 ν_e events can be selected with 1×10^{21} POT FHC data. On the other hand, the previous study could select 212 ν_e events with the same data amount since the selection was limited to stopping events. This study extended the selection to escaping events and the number of selected ν_e events has become three times larger, making it possible to gain statistics with less data. The T2K experiment plans to collect 4×10^{21} POT FHC data by 2026. With this data, 3624 ν_e candidates are expected to be selected. Among these events, 2488 are expected to be ν_e events and the statistical error is $\sqrt{3624}/2488 \simeq 2.4\%$.

7.2 Future Prospects

Shower Reconstruction with Sub-detectors

The current shower reconstruction is only done with tracks in SuperFGD. However, there are many events in which the shower is not fully contained in SuperFGD. As discussed in Sec. 6.8, the efficiency drops at the electron PID. The ν_e events that are not selected have electrons that escape with small showers. When the showers are small, it is more likely that the discriminator rejects them. In this study, TPC PID is applied to the primary tracks for escaping events. However, these events cannot be selected with TPC either since the primary track is broken due to the shower. A method to reconstruct and select EM showers with other sub-detectors is needed to further improve the efficiency.

Energy Reconstruction

Measuring the primary electron energy is crucial for cross section measurement. For events where the primary electron escapes to TPC, the momentum reconstruction can be

done with the curvature. However, if the primary electron stops in SuperFGD, the energy reconstruction will be complicated. In such events, the electrons caused by the shower must be tracked and measured with TPC or ECal when they escape SuperFGD.

Evaluating the simulation accuracy

The difference between the simulated and actual SuperFGD response must be inspected. Three parameters may affect the selection performance which are the light yield, cross-talk rate and quenching effect. The light yield for MIPs is expected to be 50 p.e. per fiber. The actual light yield will be measured with cosmic muons. Since the energy loss is one of the PID inputs, this may affect the performance. The cross-talk rate is expected to be 3.4% and it will be also checked with vertical cosmic muons. This may affect the track reconstruction. The quenching effect is a phenomenon where the relation between the energy loss and the number of produced photons becomes nonlinear when the energy loss rate is high. The empirical formula for the quenching effect is

$$\frac{dL}{dx} = S\frac{dE}{dx} \times \frac{1}{1 + B\frac{dE}{dx}} \tag{7.1}$$

which is called the Birks' law. dL/dx and dE/dx are the light yield and energy loss, S is the scintillator efficiency and B is the parameter for the quenching effect which decreases the light yield. The simulation uses $B = 0.02$ cm/MeV for SuperFGD which is an estimated value. For example, the energy loss of a proton is around 4 MeV/cm and the light yield decrease is 7% compared to the case where $B = 0$. The energy loss will be a few times larger for Bragg peaks and the light yield will decrease more. The quenching effect parameter must be measured since it may affect the proton selection. This will be done by measuring protons from ν_μ CCQE events.

Chapter 8

Conclusion

The CP violation is one of the keys to understand the asymmetry of matter and antimatter in the universe. Compared to quarks, there are few studies on leptonic CP violation. Currently, measuring neutrino oscillation is the only way to observe the CP violation in the lepton sector.

The T2K experiment is a long baseline neutrino oscillation experiment conducted in Japan. CP conservation in neutrino oscillation was rejected at a 90% confidence level from the previous data analysis. The ν_e cross-section is one of the dominant systematic uncertainties and it must be measured precisely to improve the experiment sensitivity.

T2K has upgraded ND280 to further constrain the uncertainty of neutrino interactions. SuperFGD, which is one of the new detectors, has been installed and will start collecting neutrino data in 2024. In this thesis, the particle identification in SuperFGD and other detectors are combined to select ν_e events in SuperFGD. Based on the simulation, the selection efficiency and purity for all the ν_e events are estimated to be 23% and 69%, respectively. T2K plans to collect 4×10^{21} POT neutrino beam data by 2026. With this selection method, the number of selected ν_e candidates is expected to be 3624 and the statistical uncertainty will be reduced to 2.4%.

Further study on the selection is needed since the efficiency is quite low. This is mainly due to the inefficiency of the shower discrimination. This will be improved by reconstructing the shower with other sub-detectors. Also, the difference between the simulated and actual response of SuperFGD must be studied. The light yield in particular may affect the particle identification. The accuracy of the simulation will be studied by measuring cosmic muons and ν_μ CCQE events.

Acknowledgment

List of Figures

List of Tables

Bibliography

[1] J. H. Christenson, J. W. Cronin, V. L. Fitch, and R. Turlay. Evidence for the 2π Decay of the K_2^0 Meson. *Phys. Rev. Lett.*, 13:138–140, Jul 1964. (page 4).

[2] K. Abe et al. Atmospheric neutrino oscillation analysis with external constraints in Super-Kamiokande I-IV. *Phys. Rev. D*, 97:072001, Apr 2018. (page 5).

[3] K. Abe et al. Measurements of neutrino oscillation parameters from the T2K experiment using 3.6×10^{21} protons on target. *The European Physical Journal C*, 83(9), Sep 2023. (pages 5, 6, 15).

[4] M. A. Acero et al. Improved measurement of neutrino oscillation parameters by the NOvA experiment. *Phys. Rev. D*, 106:032004, Aug 2022. (page 5).

[5] Manuela Boscolo, Jean-Pierre Delahaye, and Mark Palmer. *The Future Prospects of Muon Colliders and Neutrino Factories*, page 189–214. WORLD SCIENTIFIC, September 2019. (page 5).

[6] S. Abe et al. Precision Measurement of Neutrino Oscillation Parameters with Kam-LAND. *Phys. Rev. Lett.*, 100:221803, Jun 2008. (page 6).

[7] Yoshinari Hayato and Luke Pickering. The NEUT neutrino interaction simulation program library. *The European Physical Journal Special Topics*, 230(24):4469–4481, Oct 2021. (pages 8, 64).

[8] K. Abe et al. T2k neutrino flux prediction. *Physical Review D*, 87(1), Jan 2013. (pages 10, 11, 64).

[9] K. Abe et al. Measurement of the charged-current electron (anti-)neutrino inclusive cross-sections at the T2K off-axis near detector ND280. *J. High Energ. Phys.*, 114, Sep 2020. (pages 12, 15, 16, 25, 50, 64, 66).

[10] P.A. Amaudruz et al. The T2K fine-grained detectors. *Nuclear Instruments and Methods in Physics Research Section A: Accelerators, Spectrometers, Detectors and Associated Equipment*, 696:1–31, Dec 2012. (page 12).

[11] T2K ND280 TPC collaboration. Time Projection Chambers for the T2K Near Detectors. arXiv:1012.0865, 2010. (pages 13, 14, 64).

[12] S. Assylbekov et al. The t2k ND280 off-axis pi–zero detector. *Nuclear Instruments and Methods in Physics Research Section A: Accelerators, Spectrometers, Detectors and Associated Equipment*, 686:48–63, Sep 2012. (page 14).

[13] D. Allan et al. The electromagnetic calorimeter for the T2K near detector ND280. *Journal of Instrumentation*, 8(10):P10019–P10019, Oct 2013. (page 14).

[14] K. Abe et al. T2K ND280 Upgrade – Technical Design Report. arXiv:1901.03750, 2020. (pages 17, 19, 20, 21, 64).

[15] T. Arihara et al. Development of the in-situ calibration system using leds and light guide plates for the superfgd. *Journal of Physics: Conference Series*, 2374(1):012118, nov 2022. (pages 20, 64).

[16] Aoi Eguchi. Development of Selection Algorithms for Electron Neutrino Interaction Events with New T2K Near Detectors. Master thesis. The University of Tokyo, 2021. (pages 21, 25, 28).

[17] Davide Sgalaberna. The T2K ND280 Upgrade, Jan 2021. (pages 21, 64).

[18] J. Wolcott et al. Measurement of electron neutrino quasielastic and quasielasticlike scattering on hydrocarbon at $\langle E_\nu \rangle = 3.6$ GeV. *Physical Review Letters*, 116(8), Feb 2016. (page 25).

[19] P. Abratenko et al. First measurement of inclusive electron-neutrino and antineutrino charged current differential cross sections in charged lepton energy on argon in MicroBooNE. *Physical Review D*, 105(5), Mar 2022. (page 25).

[20] Geant4. https://geant4.web.cern.ch. (page 27).

[21] K. Abe et al. Measurement of the intrinsic electron neutrino component in the t2k neutrino beam with the ND280 detector. *Physical Review D*, 89(9), May 2014. (pages 31, 65).

[22] A. Cervera-Villanueva et al. "RecPack" a reconstruction toolkit. *Nuclear Instruments and Methods in Physics Research Section A: Accelerators, Spectrometers, Detectors and Associated Equipment*, 534(1):180–183, 2004. (page 31).